S1. Context

The IPCC Special Report on Global Warming of 1.5°C (SR1.5), published in 2018, provided an assessment of the level of human-induced warming and cumulative emissions to date (Allen et al., 2018) and the remaining carbon budget (Rogelj et al., 2018) to support the evidence base on how the world is progressing in terms of meeting aspects of the Paris Agreement. The AR6 WGI Report, published in 2021, assessed past, current and future changes of these and other key global climate indicators, as well as undertaking an assessment of the Earth's energy budget. It also updated its approach for estimating human-induced warming and global warming level. In AR6 WGI and here, reaching a level of global warming is defined as the global surface temperature change, averaged over a 20-year period, exceeding a particular level of global warming, e.g. 1.5°C global warming. Given the current rates of change and the likelihood of reaching 1.5°C of global warming in the first half of the 2030s (Lee J.-Y. et al., 2021; Lee et al., 2023; Riahi et al., 2022), it is important to have robust, trusted, and also timely climate indicators in the public domain to form an evidence base for effective science-based decision making.

S2. Emissions

Table S1 The three GHG emissions estimates and their underlying datasets.

Estimate	Source	Datasets	Reference
WGIII update	CO_2-FFI and CO_2-LULUCF	GCB v2024	Friedlingstein et al., 2025
	CH_4, N_2O	PRIMAP Hist-TP v2.6.1	Gütschow et al., 2025
	UNFCCC F-gases	CIP v2025: Climate Indicators Project (this article), with underlying data from NOAA and AGAGE inversions (see Sect. 3 main manuscript)	Main paper; Lan et al., 2025; Dutton et al., 2024; Prinn et al., 2018
WGIII update + additional sources	CO_2-FFI, CO_2-LULUCF, CH_4, N_2O and UNFCCC F-gases	As for WGIII update	Friedlingstein et al., 2025, Gütschow et al., 2025, Lan

			et al., 2025; Dutton et al., 2024; Prinn et al., 2018
	Biomass fires (CH_4 and N_2O)	GFED v4.1	van der Werf et al., 2017
	ODS F-gases	CIP v2025: Climate Indicators Project (this article), with underlying data from NOAA and AGAGE inversions (see Sect. 3 main manuscript)	Lan et al., 2025; Dutton et al., 2024; Prinn et al., 2018
	Cement carbonation	GCB v2024	Friedlingstein et al., 2025
Inventory aligned	CO_2-FFI, CH_4, N_2O and UNFCCC F-gases	PRIMAP Hist-CR v2.6.1	Gütschow et al., 2025
	CO_2-LULUCF	Grassi NGHGI v2024	Grassi et al., 2024

S2.1 Calculation of uncertainties and CO_2 equivalent emissions in Section 2

We follow the same approach for estimating uncertainties and CO_2-equivalent emissions as in AR6: CO_2-equivalent emissions were calculated using global warming potentials with a 100-year time horizon (GWP100 henceforth) from AR6 WGI Chap. 7 (Forster et al., 2021). Uncertainty ranges were based on a comparative assessment of available data and expert judgment, corresponding to a 90 % confidence interval (Minx et al., 2021): ±8 % for CO_2-FFI, ±70 % for CO_2-LULUCF, ±30 % for CH_4 and F-gases, and ±60 % for N_2O (note that the GCB assesses 1 standard deviation uncertainty for CO_2-FFI as ±5 % and for CO_2-LULUCF as ±2.6 $GtCO_2$; Friedlingstein et al., 2025). The total uncertainty was summed in quadrature, assuming independence of estimates per species/source. Reflecting these uncertainties, AR6 WGIII reported emissions to two significant figures only. Uncertainties in GWP100 metrics of roughly ±10 % were not applied (Minx et al., 2021).

S3. Greenhouse gas concentrations

Naming conventions and details for Sect. 3 of the main paper and herein follow AR6 WGI Chapter 2 (Gulev et al., 2021).

Table S2 Annual mean concentrations of well-mixed greenhouse gases in 2023, 2022, 2019, 1850 and 1750. Except for CO_2, CH_4 and N_2O, concentrations all are in parts per trillion by volume [ppt]. For halogenated gases, concentrations are stated for each gas, with equivalents for HFCs, PFCs and Montreal gases given as the radiative equivalent of the most abundant gas in each category.

Greenhouse gas	1750	1850	2019	2023	2024
CO_2 [ppm]	278.4	285.6	410.1	419.4	422.8
CH_4 [ppb]	729.2	807.6	1866.5	1922.1	1929.7
N_2O [ppb]	270.1	272.1	332.1	336.9	337.9
NF_3	0	0	2.1	3.1	3.4
SF_6	0	0	10	11.4	11.8
SO_2F_2	0	0	2.5	2.9	3
HFCs as HFC-134a-eq	**0**	**0**	**237.1**	**302.7**	**312.3**
HFC-134a	0	0	107.6	129.5	134.7
HFC-23	0	0	32.4	36.7	37.3
HFC-32	0	0	19.5	32.5	35.7
HFC-125	0	0	29.6	44.2	45.4
HFC-143a	0	0	24	31.1	30.2
HFC-152a	0	0	7.1	7.5	7.9
HFC-227ea	0	0	1.6	2.3	2.4
HFC-236fa	0	0	0.2	0.2	0.3
HFC-245fa	0	0	3.1	3.8	3.9
HFC-365mfc	0	0	1.1	1.2	1.1
HFC-43-10mee	0	0	0.3	0.3	0.3
PFCs as CF_4-eq	**34.1**	**34.1**	**109.7**	**115.8**	**117.4**
CF_4	34	34	85.5	89.4	90.4
C_2F_6	0	0	4.8	5.2	5.3
C_3F_8	0	0	0.7	0.8	0.8
c-C_4F_8	0	0	1.8	2	2.1
n-C_4F_{10}	0	0	0.2	0.2	0.2
n-C_5F_{12}	0	0	0.1	0.2	0.2
n-C_6F_{14}	0	0	0.2	0.2	0.2
i-C_6F_{14}	0	0	0.1	0.1	0.1
C_7F_{16}	0	0	0.1	0.1	0.1
C_8F_{18}	0	0	0.1	0.1	0.1
Montreal gases as CFC-12-eq	**8.5**	**8.5**	**1031.9**	**1005**	**996.1**
CFC-12	0	0	503	487.2	482.9

CFC-11	0	0	226.2	216.8	214.5
CFC-113	0	0	69.8	67.2	66.6
CFC-114	0	0	16	16	16
CFC-115	0	0	8.7	8.9	8.9
CFC-13	0	0	3.3	3.4	3.4
CFC-112	0	0	0.4	0.4	0.4
CFC-112a	0	0	0.1	0.1	0.1
CFC-113a	0	0	0.9	1.3	1.4
CFC-114a	0	0	1	1	1
HCFC-22	0	0	246.8	248.1	245.9
HCFC-141b	0	0	24.4	24.6	24.5
HCFC-142b	0	0	22.3	21.5	21.2
HCFC-133a	0	0	0.4	0.4	0.4
HCFC-31	0	0	0.1	0.1	0.1
HCFC-124	0	0	1	0.9	0.9
CH3CCl3	0	0	1.6	0.9	0.8
CCl4	0	0	78	73.9	72.9
CH3Cl	457	457	540.8	542.8	542.7
CH3Br	5.3	5.3	6.5	6.5	6.5
CH2Cl2	6.9	6.9	40.6	48.1	49.9
CHCl3	4.8	4.8	8.8	7.6	7.3
Halon-1211	0	0	3.3	2.9	2.8
Halon-1301	0	0	3.3	3.3	3.4
Halon-2402	0	0	0.4	0.4	0.4

S4. Short-Lived Climate Forcers (SLCFs)

Table S3 Emissions of the major SLCFs in 1750, 2019, 2022, 2023 and 2024 from a combination of CEDS and GFED and CAMS for the 2024 trend. Provisional estimates used in Forster et al. (2023) and Forster et al. (2024) are shown. Emissions of SO_2+SO_4 use SO_2 molecular weights. Emissions of NO_x use NO_2 molecular weights. VOCs are for the total mass.

Compound	1750	2019 (WGI)	2019 (updated with CEDS v 2025_03-18 and GFEDv4)	2022 (Forster et al., 2023)	2022 (updated with CEDS v 2025_03-18 and GFEDv4)	2023 (Forster et al., 2024)	2023 (updated with CEDS v 2025_03-18 and GFEDv4)	2024 (CEDS v 2025_03-18 and GFEDv4)

Sulphur dioxide (SO_2) + sulphate (SO_4^{2-})	2.8	84.2	80.9	75.3	70.6	79.1	72.7	71.2
Black carbon (BC)	2.1	7.5	7.3	6.8	6.7	7.3	7.6	7.5
Organic carbon (OC)	15.5	34.2	33.0	25.8	25.6	40.7	41.0	36.1
Ammonia (NH_3)	6.6	67.6	66.3	67.3	66.8	71.1	72.7	70.6
Oxides of nitrogen (NO_x)	19.4	141.7	133.6	130.4	123.2	139.4	128.4	130.4
Volatile organic compounds (VOCs)	60.9	217.3	204.8	183.9	176.4	228.1	224.1	212.7
Carbon monoxide (CO)	348.4	853.8	816.1	686.4	665.4	917.5	896.0	845.3

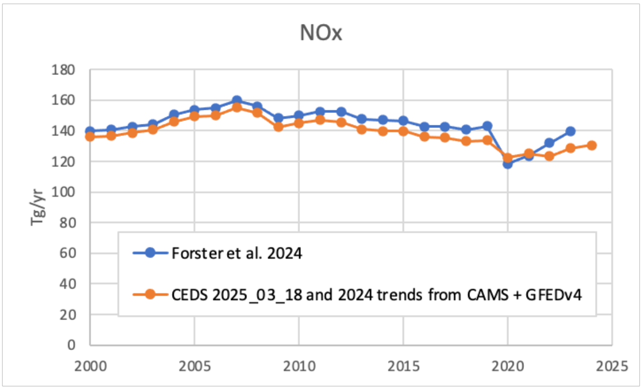

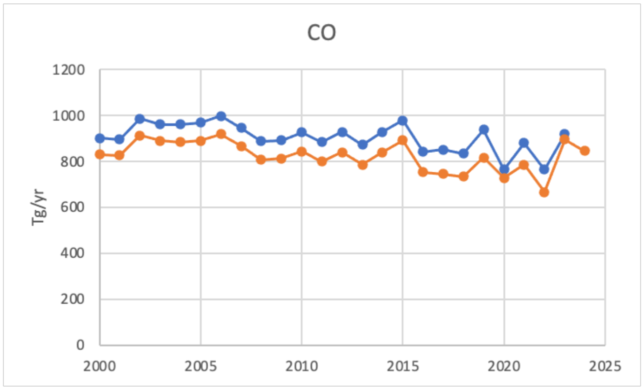

Figure S1 Comparison of short-lived climate forcer emissions from Forster et al. (2024) (blue) and the most recent update of CEDS and GFED through 2023, with 2024 trend from CAMS (orange). (Granier et al., 2019; Jalkanen et al. 2012, 2016; Johansson et al., 2017).

S5. Effective radiative forcing (ERF)

S5.1 Well-mixed greenhouse gas ERF methods

Radiative forcing (RF) from CO_2, CH_4 and N_2O use the simplified formulas from concentrations in Meinshausen et al. (2020), derived from an updated functional fit to Etminan et al. (2016) line-by-line radiative transfer results. These formulas are, to first order, logarithmic with CO_2 concentrations and a square-root dependence for CH_4 and N_2O, with additional corrections and radiative band overlaps between gases. RF is converted to ERF using scaling factors (1.05, 0.86 and 1.07 for CO_2, CH_4, N_2O respectively) that account for tropospheric and land-surface rapid adjustments (Smith et al., 2018a; Hodnebrog et al., 2020a). ERF from other GHGs is assumed to scale linearly with their concentration based on their radiative efficiencies expressed in W m^{-2} ppb^{-1} (Hodnebrog et al., 2020b, Smith et al., 2021b). A scaling factor translating RF to ERF is implemented for CFC-11 (1.13) and CFC-12 (1.12) (Hodnebrog et al., 2020a), whereas no model evidence exists to treat ERF differently to RF for other halogenated gases.

Relative uncertainties in the ERF for CO_2 (± 12%), CH_4 (± 20%) and N_2O (± 14%) are unchanged from AR6. These stem from a combination of spectroscopic uncertainties and uncertainties in the adjustment terms converting RF to ERF; uncertainties in the volume mixing concentrations themselves are assessed to be small (Sect. 2). Uncertainties in the ERF from halogenated gases are treated individually and are assessed as ±19% for gases with a lifetime of 5 or more years and ±26% for shorter lifetime gases. In AR6, a ±19% uncertainty was applied to the sum of the ERF from all halogenated gases. To maintain a consistent uncertainty range across the sum of ERF from halogenated gases with AR6, we inflate the uncertainty in each individual gas by a factor of 2.05. Uncertainties are applied by scaling the full ERF time series for each gas.

S5.2 Aerosol ERF methods

Aerosol ERF is a combination of contributions from aerosol-radiation interactions (ERFari) and aerosol-cloud interactions (ERFaci).

S5.2.1 Aerosol-radiation interactions

Contributions to ERFari are assumed to scale linearly with certain SLCF emissions in Sect. 3 (SO_2, BC, OC, NH_3, NOx and VOC) or concentrations (CH_4, N_2O and ozone-depleting halocarbons) of primary aerosols and chemically active precursor species. The coefficients converting emissions or concentrations of each SLCF into ERF and its uncertainty come from Chapter 6 of AR6 WGI (Szopa et al., 2021), originally from CMIP6 AerChemMIP models (Thornhill et al., 2021a). We scale these coefficients to reproduce the headline AR6 WGI ERFari assessment of -0.3 W m^{-2} from 1750 to 2005-2014. Uncertainties are applied as a scale factor for each species and applied to the whole time series.

The inclusion of more species that affect ERFari differs from the AR6 WGI calculation of ERFari in Chapter 7, which only used SO_2, BC, OC and NH_3 (Smith et al., 2021b). In the update, these four species remain the dominant aerosol and aerosol precursors. Additionally, these coefficients have changed slightly due to switching to CMIP6 era data. In AR6, the coefficients scaling emissions to ERF for SO_2, BC, OC and NH_3 were provided by CMIP5-era models (Myhre et al., 2013a). The additional coefficients and slight changes to their magnitude had an imperceptible effect on the results but have been included to align with current best practice. This might be important in future years as NOx and VOC precursors might make up a larger fraction of ERFari.

S5.2.2 Aerosol-cloud interactions

ERFaci is estimated by assuming a logarithmic relationship with the change in cloud droplet number concentration (CDNC) as

$$\mathrm{ERFaci} = \beta \log\left(1 + \Delta \mathrm{CDNC}\right) \qquad \text{(S1)}$$

$$\Delta \mathrm{CDNC} = s_{\mathrm{SO2}} \Delta E_{\mathrm{SO2}} + s_{\mathrm{BC}} \Delta E_{\mathrm{BC}} + s_{\mathrm{OC}} \Delta E_{\mathrm{OC}} \qquad \text{(S2)}$$

where s_{SO2}, s_{BC} and s_{OC} are sensitivities of the change in CDNC with the change in emissions of SO_2, BC and OC respectively (ΔE). This relationship is fit to estimates of ERFaci in 13 CMIP6 models contributing results to the piClim-histaer and histSST-piAer experiments of RFMIP and AerChemMIP, respectively, to CMIP6 (Smith et al., 2024). The ERFaci in these 13 models is estimated using the Approximate Partial Radiative Perturbation (APRP) method (Taylor et al., 2007; Zelinka et al., 2014; Zelinka et al., 2023a).

The s_{SO2}, s_{BC} and s_{OC} values from each model are combined into a kernel density estimate and sampled 100,000 times to provide a CMIP6-informed distribution of these parameters. To obtain β for each sample given (s_{SO2}, s_{BC}, s_{OC}) a target ERFaci value for 1750 to 2005-2014 is drawn from the headline AR6 distribution of -1.0 [-1.7 to -0.3] W m^{-2} and eq. (S1) rearranged. This follows a very similar procedure to AR6 and is based on Smith et al. (2021a) with three updates. Firstly, the relationships in eqs. (S1) and (S2) are slightly updated and simplified (Smith et al., 2024). Secondly, an additional two CMIP6 models have become available since the AR6 WG1 assessment which expands the sampling pool for coefficients from 11 to 13. Thirdly, a slight error in computing ERFaci from APRP from the CMIP6 models in Smith et al. (2021a) has been corrected (Zelinka et al., 2023b).

S5.3 Ozone ERF methods

In AR6 WGI Chapter 7, the ozone ERF is derived from CMIP6 model-based estimates (Skeie et al., 2020) from 1850 to 2014, to infer the sensitivity of ozone RF to emissions of NOx, VOC and CO, concentrations of CH_4, N_2O and ozone-depleting halogens, and global mean surface temperature (GMST) anomaly. These factors can be found in Table 7.SM.3 of AR6. In CMIP6, experimental results that vary CO and VOC emissions separately are not available, so individual contributions from CO and VOC to the CO+VOC total are based on their fractional contributions from ACCMIP (CMIP5-era) models in Stevenson et al. (2013). To compute the ozone ERF we thus use the radiative efficiencies for ozone ERF and the scale factor to CH_4, N_2O and ozone-depleting halogens concentration changes discussed in the paper and CO, NMVOC and NOx emission changes discussed in the paper. For the global mean temperature contribution to ozone forcing (in terms of W m^{-2} K^{-1}), we use the model responses to ozone forcing per degree warming in chemistry-enabled models in abrupt-4xCO2 experiments (Thornhill et al., 2021b), and apply this factor to the observed GMST anomaly from Sect. 7. Following AR6, we do not differentiate between stratospheric and tropospheric ozone, and we also assume that ERF is the same as RF as there is limited model evidence to suggest otherwise.

S5.4 ERF from land use change and irrigation

In Forster et al., (2024), ERF from land use and irrigation was scaled with cumulative CO_2 emissions from AFOLU from 1750, as the IPCC AR6 assessment from Ghimire et al. (2014) did not extend beyond 2005, and the IPCC assessment used cumulative AFOLU CO_2 emissions to estimate land use and irrigation ERF from 2005 to 2019. In IGCC 2024, we use land use transitions from the Land Use Harmonization v2 (LUH2) dataset (Hurtt et al., 2020) updated for the Global Carbon Budget (GCB) 2024 (Chini et al., 2021; Friedlingstein et al., 2025) using cropland and grazing land data from HYDE3.4 (Klein Goldewijk et al., 2017) that itself merges the latest FAO state-level data with MapBiomas satellite-based estimates for Brazil and Indonesia (Souza et al., 2020) and another recent estimate for China (Yu et al., 2022). This constitutes an update to the Ghimire et al. (2014) data that used LUH1, using the satellite-derived albedo-related parameters of Ouyang et al. (2022) and providing data for 1750-2023, which we extrapolate one year to 2024. The resulting global ERF is scaled by a factor of 1.28 to recover the Ghimire et al. (2014) surface reflectance assessment of -0.15 W m^{-2} in 2005 relative to 1750 to ensure consistency with the AR6. For irrigation, we assume the forcing scales with the area of land irrigated. We create a timeseries of this irrigated land area, using FAOSTAT (FAO, 2024) from 1961-2022, and Angelakis et al. (2021) to extend back to 1750. Angelakis et al.

(2021) provide data points from 1900 in their Figure 21, and give a value for 1800 in the text. We assume the 1800 value (8 megahectares as compared to 354 megahectares in 2022) applies to 1750 and apply a cubic spline fit to produce a time series of irrigated area from 1750 to 1961 which is scaled to match the 1961 FAOSTAT irrigated area. The irrigated area in 2019 is assumed to result in the AR6 assessment of irrigation forcing of -0.05 W m^{-2} in 2019 (having its roots in Sherwood et al., 2018), and irrigation forcing is linear with irrigated area relative to this benchmark. We note that since the publication of AR6, more Earth System models incorporating transient historical irrigation are available (Yao et al., 2025), and could be used to provide an assessment of the ERF of irrigation in future.

S5.5 ERF from other anthropogenic forcers

Minor categories of anthropogenic forcers include contributions from land use and land use change other than via GHG emissions, aviation contrails and contrail-induced cirrus, stratospheric water vapour from methane oxidation, and light absorbing particles on snow and ice.

The methodology to estimate ERF from land use and land-use change, including irrigation, has been updated to be more consistent with AR6 (Sect. 5) We anchor the 1750-2019 assessment to be the same as AR6 at -0.15 [-0.25 to -0.05] W m^{-2} for the ERF from surface albedo changes and -0.05 [-0.10 to +0.05] W m^{-2} for irrigation under this updated methodology. Stratospheric water vapour from methane oxidation was assessed to be 0.05 [0.00 to 0.10] W m^{-2} in AR6 for 1750-2019, and is assumed to change linearly with changes in methane concentration.

The ERF from light absorbing particles on snow and ice (LAPSI) is assumed to scale with emissions of black carbon. As in AR6, the contribution from brown carbon is assumed to be negligible. We align the coefficient that converts BC emissions to ERF from LAPSI to match the 0.08 [0.00 to 0.18] W m^{-2} assessment in AR6 for 1750-2019.

To estimate ERF from aviation contrails and contrail-induced cirrus in AR6, emissions of NOx from the aviation sector in CEDS were scaled to reproduce an ERF of 0.0574 [0.019 to 0.098] W m^{-2} for 1750-2018 as assessed in Lee D. S. et al. (2021). We more closely follow the original methods of Lee D. S. et al. (2021) in this update to base our ERF estimates as closely as possible on aviation activity data. The Lee D.S. et al. (2021) ERF time series is extended to 2022 based on aviation fuel consumption from the International Energy Agency's (IEA) World Oil Statistics (2024). For 2023 and 2024, we use fuel consumption data from the International Air Transport Association (IATA, 2024).

S5.5 Methods for estimating natural forcing

Natural forcing is composed of solar irradiance and volcanic eruptions.

S5.5.1 Solar irradiance

The method to compute solar forcing is unchanged from AR6, using a composite time series prepared for PMIP4 (Jungclaus et al., 2017) and CMIP6 (Matthes et al., 2017). The headline assessment of solar ERF is based on the most recent solar cycle (2009-2019), which is unchanged from AR6. Solar ERF estimates are computed relative to complete solar cycles encompassing the full “pre-industrial” period where proxy data exists (6754 BCE to 1745 CE). The CMIP7 solar forcing time series for the historical period (1850–2023) is now available (Funke et al., 2024). However, it has changed from the CMIP6 time series and does not seamlessly transition to the pre-1850 period including the last several thousand years, nor does it extend forward to include 2024. In future editions of IGCC, the CMIP7 solar forcing product could be used if the data spans the appropriate periods.

S5.5.2 Volcanic

Volcanic ERF consists of contributions from stratospheric sulphate aerosol optical depth (sAOD; a negative forcing) and stratospheric water vapour (sWV, a positive forcing). The sAOD time series (at a nominal wavelength of 550 nm) is constructed from a combination of four datasets which have temporal overlap. We use ice-core deposition data from HolVol v1.0 (Sigl et al., 2022) for 9500 BCE to 1749 CE. For 1750 to 2023 we use the CMIP7 volcanic sAOD dataset (Durack et al., 2025) using the 550 nm spectral band, which is an update from IGCC 2023 that used the CMIP6 volcanic sAOD dataset. There is a seamless transition between HolVol and CMIP7 in 1750, so no blending of datasets was required. In previous editions of IGCC, we used the Global Space-based Stratospheric Aerosol Climatology (GloSSAC) product of sAOD which provided data until the penultimate year (Thomason et al., 2018), however, with the availability of the CMIP7 dataset to 2023, GloSSAC is not required directly in this year’s IGCC. Additionally, the CMIP7 dataset incorporates GloSSAC from 1979 to 2023. For 2024, we use the Ozone Mapping and Profiling Limb Profiler (OMPS LP) Level 3 aerosol optical depth at 745 nm, which is scaled to achieve the same time mean sAOD as GloSSAC v2.22 (Kovilakam et al., 2020) in the overlapping 2013-2023 period as a single Ångstrom exponent is not suggested for this conversion. The 745 nm band from OMPS-LP is used as this is reported to be more stable than the bands closer to 550 nm from OMPS LP (Taha et al., 2021). For comparison we estimate the 550 nm sAOD from GloSSAC v2.22 using the 525 nm band and an Ångstrom exponent of -2.33, and we find good correspondence to the CMIP7 sAOD time series for the 1979-2023 common period. Therefore, while GloSSAC is not used directly this year, it is used as an anchor and reference for both the CMIP7 and OMPS-LP datasets. sAOD is converted to a radiative effect using a scaling factor of -20 ± 5 as in AR6 (Smith et al., 2021b) that is representative of CMIP5 and CMIP6 models. ERF is calculated with reference to the change in this radiative effect since "pre-industrial", defined as the mean of all available years before 1750 CE. In other words, the mean of the pre-1750 period is defined as zero forcing.

The January 2022 eruption of Hunga Tonga-Hunga Ha'apai (HTHH) was an exceptional episode in that it emitted large amounts of water vapour into the stratosphere (Millán et al., 2022; Sellitto et al., 2022). Jenkins et al. (2023) determined the HTHH eruption increased volcanic ERF in 2022 by +0.12 W m^{-2} due to sWV. In IGCC 2024 we update this value from Jenkins et al. (2023), which used an idealised injection of water vapour, to use direct satellite retrievals of water vapour from the Microwave Limb Sounder (MLS) data on board the Aura platform. Using the MLS data in place of the Jenkins et al. (2023) spatial distribution, we update the 2022 volcanic sWV ERF to +0.14 W m^{-2}, and find that in the MLS data the stratospheric water vapour plume persists into 2023 (+0.18 W m^{-2}) and 2024 (+0.15 W m^{-2}) (Fig. S2). These water vapour forcings are calculated in a similar fashion to in Jenkins et al. (2023), by implementing the stratospheric water vapour in 2022, 2023 and 2024 from MLS against a climatology derived from MLS using the 2004-2021 years. The instantaneous radiative forcing at the tropopause is calculated using the SOCRATES radiative transfer model (Edwards and Slingo, 1996), against a background climatology (atmospheric temperatures, humidity, cloud profiles, ozone profiles, surface albedo and surface temperature) taken from ECMWF ERA5 reanalysis (Hersbach et al., 2020). From the CMIP7 and GloSSAC data the peak addition of stratospheric aerosols was around 0.007 optical depth units in the global mean, resulting in a peak volcanic aerosol forcing of –0.14 W m^{-2} in mid-2022 relative to the pre-HTHH baseline that decayed away with an e-folding lifetime of around 18 months. We conclude using this analysis that the net HTHH ERF from both sAOD and sWV was positive (but small) in 2022, 2023 and 2024, and attempting to back out HTHH from other small eruptions gives a best estimate ERF for HTHH in isolation of +0.03 W m^{-2} in 2022, +0.10 W m^{-2} in 2023 and +0.10 W m^{-2} in 2024. This is in contrast to other studies that assess a net negative (Gupta et al., 2025) or zero (Schoeberl et al., 2024) impact of HTHH, using different methods.

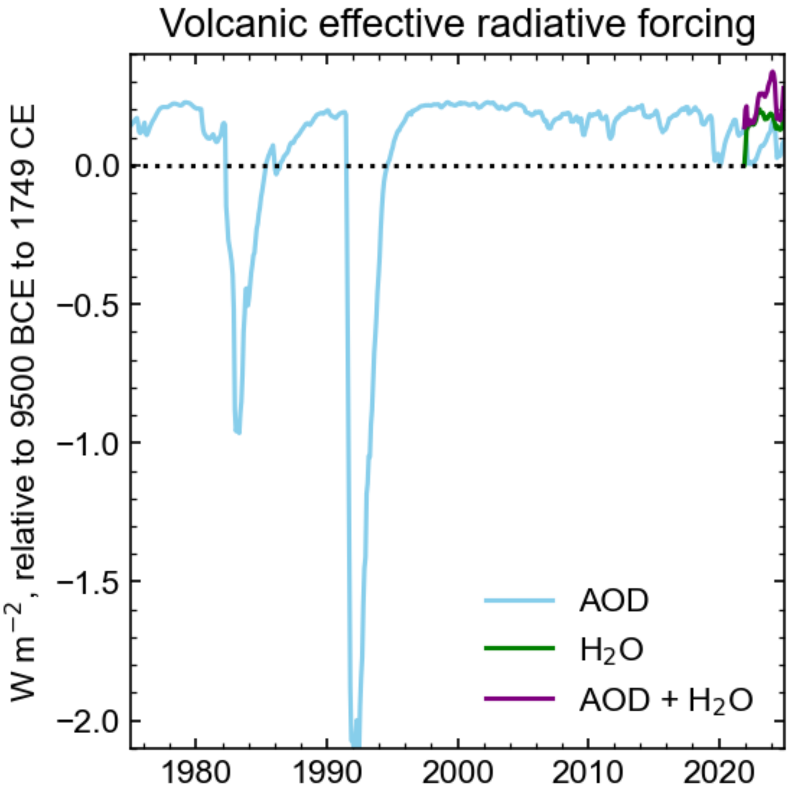

Figure S2 Volcanic effective radiative forcing from 1975 to present relative to the pre-1750 baseline. The impact of including stratospheric water vapour from Hunga Tonga-Hunga Ha'apai (green) can be observed in 2022, 2023 and 2024 by increasing the net volcanic ERF above the background level (purple).

S6. Earth energy imbalance

While changes in EEI have been effectively monitored at the top of the atmosphere by satellites since the mid-2000s, we rely on estimates of OHC change to determine the absolute magnitude of EEI and its evolution on inter-annual to multi-decadal time series. The AR6 assessment of ocean heat content change for the 0–2000 m layer was based on global annual mean time series from five ocean heat content datasets: IAP (Cheng et al., 2017), Domingues et al. (2008), EN4 (Good et al., 2013), JMA (Ishii et al., 2017) and NCEI (Levitus et al., 2012). Four of these datasets routinely provide updated OHC time series for the BAMS State of the Climate report, and all are used for the GCOS Earth heat inventory (von Schuckmann et al., 2020, 2023a) and the annual WMO State of the Global Climate report. The uncertainty assessment for the 0–2000 m layer used the ensemble method described by Palmer et al. (2021) that separately accounts for parametric (referred to in the plots below as “mapping uncertainty”) and structural uncertainty. The OHC change >2000 m and associated uncertainty were assessed based on trend analysis of the available hydrographic data following Purkey and Johnson (2010). All five of the datasets used for the 0–2000 m OHC assessment are now updated at least annually and should in principle support an AR6 assessment time series update within the first few months of each year. There is potential to increase the observational ensemble used in the assessment by supplementing this set with additional data products that are also available annually for future updates. A full propagation of uncertainties across all heat inventory components depends on the specific choice of time period, and different estimates are not directly comparable. Therefore, we take a simple pragmatic approach, using the total ocean heat content uncertainty as a proxy for the total uncertainty, since this term is 2 orders of magnitude larger than the other terms (Forster et al., 2021). To provide estimates of the EEI up to the year 2024, we scale up the values of OHC change in 2021, 2022, 2023 and 2024 to reflect the ~ 90 % contribution of the ocean to changes in the Earth heat inventory. The EEI is then simply computed as the difference in global energy inventory over each period, converted to units of watts per square metre (W m^{-2}) using the surface area of the Earth and the elapsed time. The uncertainties in the global energy inventory for the end-point years are assumed to be independent and added in quadrature, following the approach used in AR6 (Forster et al., 2021). Estimates of EEI should also account for the other elements of the Earth heat inventory, i.e. the atmospheric warming, the latent heat of global ice loss and heating of the continental land surface (Forster et al., 2021; Cuesta-Valero et al., 2021, 2023a; Steiner et al., 2020; Nitzbon et al., 2022a; Vanderkelen et al., 2020; Adusumilli et al., 2022). Some of these components of the Earth heat inventory are routinely updated by a community-based initiative reported in von Schuckmann et al. (2020, 2023a). However, in the absence of annual updates to all heat inventory components, a pragmatic approach is to use recent OHC change as a proxy for EEI, scaling the value up as required based on historical partitioning between Earth system components.

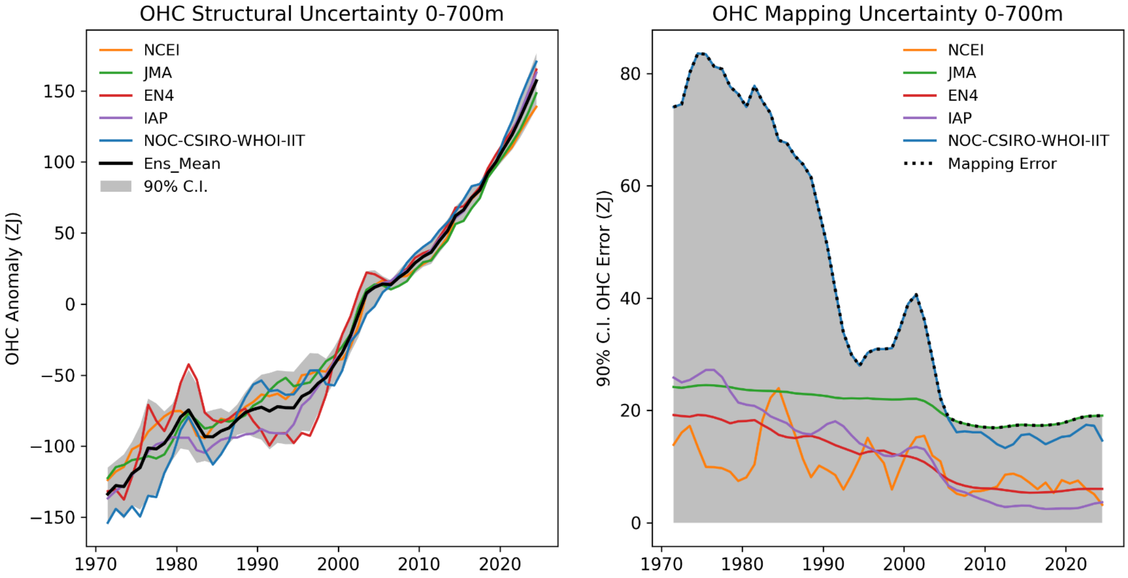

Figure S3 (Left) Ocean heat content timeseries for the 0-700 m layer with the estimate of structural uncertainty indicated by the grey shaded region and expressed as a 90% confidence interval (*very likely* range) in units of Zetta Joules (1 ZJ = 10^{21} Joules). (Right) Individual estimates of the mapping uncertainty with the ensemble mapping uncertainty (the maximum across all available estimates) shown by the dotted line and grey shaded region. Mapping uncertainty is expressed as a 90% confidence interval (*very likely* range) in units of Zetta Joules (1 ZJ = 10^{21} Joules).

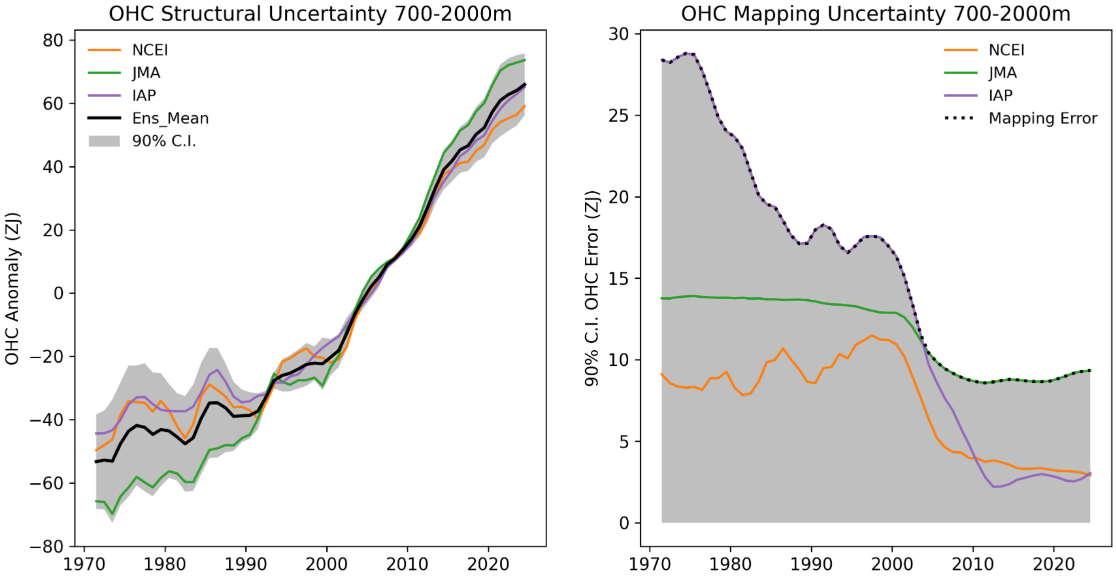

Figure S4 As Figure S3 but for ocean heat content in the 700-2000 m layer.

S7. Global surface temperature

Surface temperature information on land and sea is available with low latency through WMO distribution channels, with monthly station data from a substantial number of stations reported within a few days of the end of the month. Sea-surface temperature data from ships and buoys are gathered from the Global Telecommunication System with a short delay. These are consolidated into global data sets by a number of institutions, making it feasible to report GMST updates within a few weeks of the end of the period of interest. The number of reporting locations on land with near-real time data available for reporting for the most recent periods is typically less than that available for historical data, as not all observation sites report recent data reliably, but this lower observation density only slightly increases the uncertainty in estimates of recent annual GMST compared with the past 20-30 years (Trewin et al., 2021).

The GMST assessment in AR6 was largely based on four datasets: HadCRUT5 (Morice et al., 2021), Berkeley Earth (Rohde and Hausfather, 2020), NOAAGlobalTemp - Interim (Vose et al., 2021) and Kadow et al. (2020). The four GMST datasets were chosen by virtue of being quasi globally complete, having data back to 1850, using the most recent generation of SST analyses and using analysed (rather than climatological) values over sea ice. The first two of these are routinely updated operationally, with data for each year becoming available in the first few weeks of the following year. NOAAGlobalTemp - Interim was not updated operationally at the time AR6 was published but became NOAA's main operational GMST dataset (under the name NOAAGlobalTemp 5.1) as of January 2023. All three datasets are updated and published monthly. The dataset by Kadow et al. is updated on an ad hoc basis by the authors. A fifth data set, China - Mean Surface Temperature (China-MST) (Sun et al., 2021), which meets all the GMST dataset criteria except for treatment of sea ice areas, is used both in AR6 and here for global temperatures over land areas only. Although the version of the Kadow et al. (2020) dataset reported in that paper used HadCRUT4 as its base, the version used in AR6 and subsequently used HadCRUT5 as its base.

In 2023, there was a significant version change to NOAAGlobalTemp (now version 6.0.0). This is the current operational version and is used in this paper. This uses a new artificial neural network approach to reconstruct temperatures over land (Huang et al., 2022) in place of the empirical orthogonal teleconnection approach used in version 5.1. This change has little impact on long-term trends at global scale since the low-frequency component in the land surface air temperature (LSAT) reconstruction has not changed, but has a substantial impact on spatial and short-term temporal variability. Version 6.0.0 shows approximately 0.01 °C less warming from 1850-1900 to recent time periods (such as 2013-2022) than version 5.1, principally due to differences in the early part of the 1850-1900 baseline period. A new version of the ERSST sea surface temperature analysis (v6) has been developed (Huang et al., 2025), but as of March 2025, NOAAGlobalTemp 6.0.0 still uses ERSSTv5 as its SST component.

To date, all four GMST datasets remain supported, and those version changes which have occurred since AR6 have not had a material impact on long-term temperature changes, but it is likely that more substantive version changes will occur to one or more over time, potentially leading to differences from the AR6. Version changes to date since AR6 have resulted in the warming from 1850-1900 to 2011-2020, 2010-2019 and 2001-2020 each being 0.01 °C greater in the most recent dataset versions than that reported in AR6.

A new version of the China-MST dataset (v3.0) has been developed and is used as part of the land component of the assessment of this paper. The land component of this uses the C-LSAT 2.1 dataset (Xu et al., 2025). Compared with earlier versions, C-LSAT 2.1 has substantially more stations and a substantially greater areal data coverage, as well as new homogenisation methods. China-MST v3.0 shows more warming over the common 1850-1900 to 2014-2023 period than the v2.0 version used in 2023 and earlier, with warming of 1.61 °C in v3.0 compared with 1.53 °C in v2.0. This change brings China-MST into closer alignment with the other four datasets although it still shows the least amount of warming of the five.

The key differences between the AR6 datasets and those used in the annual WMO and BAMS State of the Climate reports are that WMO and BAMS also incorporate reanalyses (ERA5 and JRA-3Q, which superseded JRA-55 during 2024). These reports also include the GISTEMP (Lenssen et al., 2019) dataset (excluded by AR6 because it starts in 1880) but do not include the dataset by Kadow et al. (as that is not updated operationally).

The GMST values used in AR6 were calculated from the gridded data sets produced by the data providers, using a consistent methodology - calculating the mean anomaly for each of the northern and southern hemisphere as a latitude-weighted mean of available gridpoint values, then defining the global mean anomaly as the mean of the two hemispheric values. (This is equivalent to the method used by the Met Office Hadley Centre to report global values from HadCRUT5). The values thus calculated may differ from those reported by the data providers themselves, due to different averaging methodologies. Although the difference is less pronounced in the AR6 datasets than in earlier generations of datasets, there are more gridpoints with missing data in the Southern Hemisphere than the Northern (particularly before an observation network was established on Antarctica in the 1950s), and using hemispheric means ensures that the two hemispheres are equally weighted.

The uncertainty assessment in AR6 combines the spread of the individual datasets with uncertainties derived from ensembles for HadCRUT5 and an earlier version of NOAAGlobalTemp, with the other two datasets assumed to have the same uncertainty as HadCRUT5. HadCRUT5 is the only one of the datasets for which regularly updated ensembles are currently produced, limiting the extent to which uncertainty assessments can be regularly updated from those used in AR6. In this update it was assumed that the width of the confidence interval for each individual dataset was the same as that used in AR6.

A number of new global temperature products have been published in the last year (e.g. Chan et al., 2024; Calvert, 2024). It is anticipated that there will be a review over the coming year of the datasets used in global temperature assessment, both in forthcoming versions of this publication (and ultimately the IPCC AR7) and in WMO reporting.

2023 and 2024 temperature anomalies

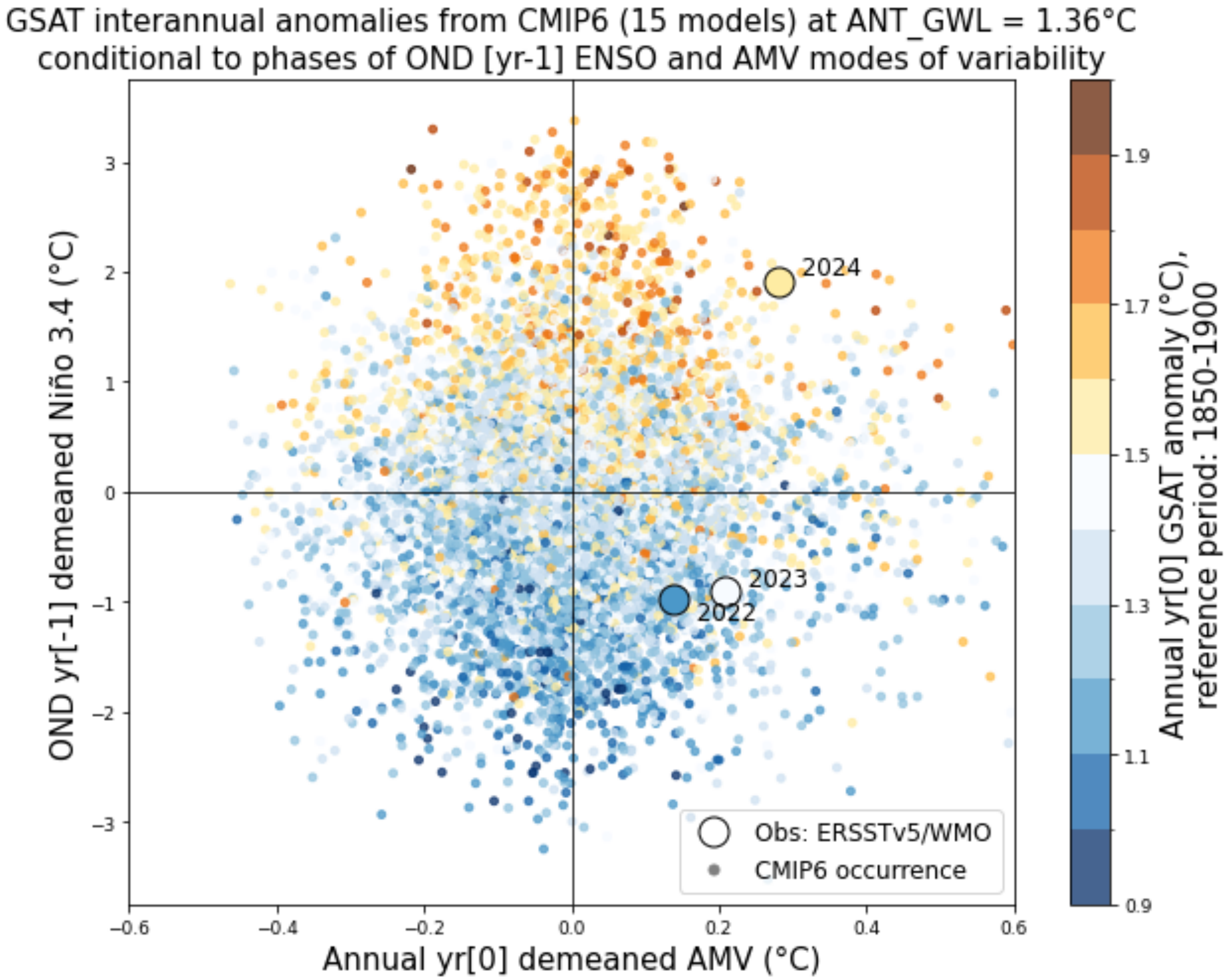

Figure S5 Global surface air temperature (GSAT) interannual anomalies from CMIP6 models (plain coloured dots) at anthropogenically-forced global warming (ANT_GWL) equal to 1.36ºC as a function of ENSO estimated by Oct-Dec mean of SST(y-axis) and AMV (x-axis). Larger dots stand for 2022, 2023 and 2024 observed values from ERSSTv5 for the modes of variability and from WMO consolidated values for GSAT. SST Anomalies for the modes of variability are calculated from the residual of SST obtained after removing the modelled forced response estimated as model ensemble mean.

While comprehensive syntheses have yet to be published, we provide a preliminary estimate of the contribution of different factors by combining the results of recent studies of their respective forcings using the FaIR climate model (Leach et al., 2021)

(Figure S6). We calculate the residuals of 0.18 ºC and 0.26 ºC for 2023 and 2024, respectively, relative to an expectation of smoothly rising temperatures calculated over the period prior through to the end of 2022 using a locally linear regression with a bandwidth of 20 years (WMO, 2025). This is not a full attribution study; the results are rather presented with associated caveats to provide a possible explanation of the anomalous temperatures in 2023 and 2024 compared to prior years.

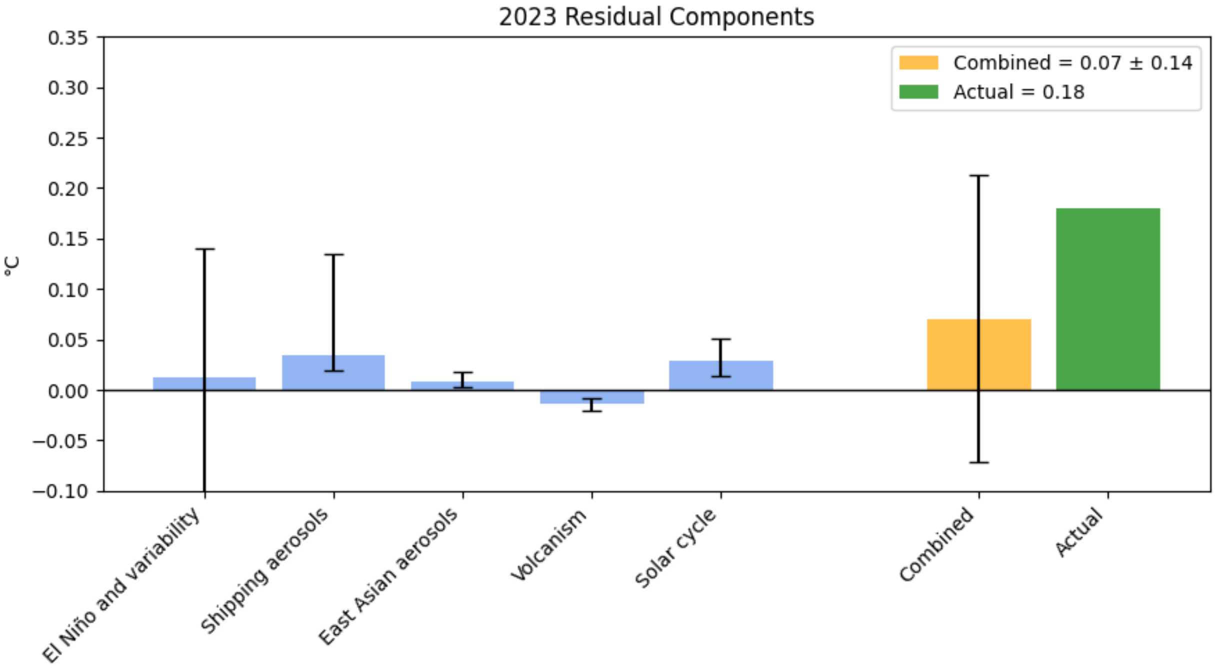
2023 Residual Components
°C
0.35
0.30
0.25
0.20
0.15
0.10
0.05
0.00
−0.05
−0.10
Combined = 0.07 ± 0.14
Actual = 0.18
El Niño and variability
Shipping aerosols
East Asian aerosols
Volcanism
Solar cycle
Combined
Actual

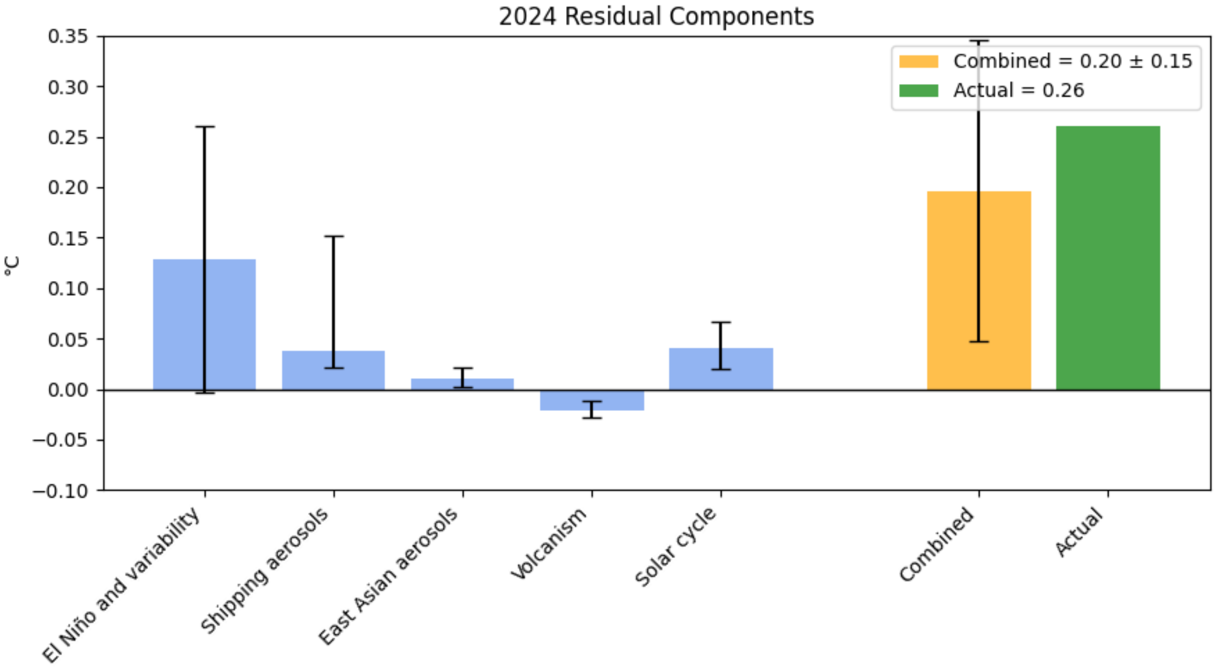
2024 Residual Components
°C
0.35
0.30
0.25
0.20
0.15
0.10
0.05
0.00
−0.05
−0.10
Combined = 0.20 ± 0.15
Actual = 0.26
El Niño and variability
Shipping aerosols
East Asian aerosols
Volcanism
Solar cycle
Combined
Actual

Figure S6 Assessed contributions to 2023 and 2024 global surface temperature residuals relative to the expected warming approach described above. The combined bar shows the combination of individual contributions, with uncertainties added in quadrature. Note that aerosol-related factors reflect declines in aerosol emissions that were previously masking warming. Actual residuals are shown in green.

The impact of ENSO on the temperatures can be estimated in multiple ways. A linear regression of the annual mean relative anomaly on the Feb/Mar Niño 3.4 index suggests an impact of −0.07 ºC, 0.01 ºC and 0.13 ºC for 2022, 2023 and 2024 respectively (95% CI, ±0.13 ºC). It is important to note that the uncertainties in the ENSO response estimated here also incorporate other sources of unforced internal (modes of variability in other basins like AMV), and potentially some forced variability, and the bar in Figure S6 is labelled "El Niño and variability" to reflect this. While some results from pre-industrial control climate model simulations (Raghuraman et al., 2024) suggest a transition from triple-dip La Niña to El Niño can produce an anomalous jump of up to 0.25 ºC in the year of transition, but it is unclear how to apply this to 2023 since one would need to condition the effect on the ENSO change that was actually experienced.

The IMO regulation change in 2020 led to a quick reduction of about 8.4 TgSO_2/yr and a step change of radiative forcing between 0.08 and 0.14 Wm^{-2}, estimated from a review of seven studies to-date: Gettelman et al, 2024; Jordan and Henry, 2024; Quaglia and Visoni, 2024; Yoshioka et al, 2024; Yuan et al, 2024; Watson-Parris et al, 2024; Skeie et al, 2024. An eighth study (Hansen et al., 2025) finds a much higher forcing value of 0.5 Wm^{-2}. The median temperature impacts across these different forcing estimates were calculated as 0.03 ºC (95% CI of 0.02 ºC to 0.14 ºC) in 2023 and 0.04 ºC (0.02 ºC to 0.15 ºC) in 2024 using FaIR, with the Hansen et al. forcing estimate responsible for the high upper bound. The latter is partly taken into account in SSP scenarios used in the above-documented probability of occurrence of the 2024 event based on CMIP6 (Szopa et al., 2021).

Chinese sulphate aerosol emissions have fallen sharply from their peak in 2006 (38 TgSO2/yr), down 39% by 2014 (23 TgSO2/yr), and an additional 56% through 2022 (10 TgSO2/yr) (CEDS 2024). On its own this would lead to additional radiative forcing of 0.14 Wm^{-2} and a warming of 0.06 ºC (±0.04 ºC) in 2023 compared to a world where East Asian harmful aerosol emissions remained at 2006 levels, based on FaIR calculations performed here. But some of this decline will have already affected the long-term trends, and so the anomaly in 2023 and 2024 relative to 2020 is only 0.01 ºC (calculated using FaIR).

The HTHH event added both SO_2 and water vapor to the stratosphere (up to 56 km in altitude). SO_2 was rapidly oxidized in sulphate aerosols, whose effects dominated the radiative forcing for the first two years after the eruption, and so the net radiative forcing at the tropopause was likely negative; the combination of HTHH and subsequent volcanism resulted in −0.04 Wm^{-2} and −0.15 Wm^{-2} in 2022 and 2023 respectively (Schoeberl et al., 2024), implying a temperature impact of -0.02 ºC (-0.01 ºC to -0.03 ºC) calculated using FaIR.

Solar cycle 25 was both slightly earlier and slightly stronger than prior expectations, and the impact of the Total Solar Irradiance (TSI) anomaly of 0.97 Wm^{-2} in 2023 relative to the mean of the prior 20 years is a radiative forcing of approximately 0.17 Wm^{-2} and an estimated global mean surface temperatures impact of 0.03 ºC (0.01 ºC to 0.05 ºC) in 2023 and 0.04 ºC (0.02 ºC to 0.07 ºC) in 2024 calculated using FaIR.

In total, the additional radiative forcings in recent years and consequent warming combined with the impact of ENSO come close to explaining the residuals taking into account the uncertainties, though more so in 2024 than in 2023. While the effects of ENSO and other modes of internal variability (especially in the Atlantic where 2023 was extreme (Guinaldo et al., 2025)), changes in the solar cycle, and volcanism are likely to subside, the additional warming unmasked by declining shipping and East Asian aerosol emissions will persist.

S8 Human-induced global warming

S8.1 Estimates of global surface temperature: GMST and GSAT in attributed warming assessments

AR6 WGI (Chap. 2 Cross-Chap. Box 2.3, Gulev et al., 2021) described how global mean surface air temperature (GSAT), as is typically diagnosed from climate models, is physically distinct from the global mean surface temperature (GMST) estimated from observations, which generally combine measurements of near-surface temperature over land and in some cases over ice, with measurements of sea surface temperature over the ocean. Gulev et al. (2021) assessed with high confidence that long-term trends in the two indicators differ by less than 10 %. However, based on conflicting lines of evidence from climate models and direct observations, the former showing stronger warming of GSAT compared to GMST, the latter tending to show the opposite, there is low confidence in the sign of the difference in trends. Therefore, with medium confidence, in AR6 WGI Chap. 3 (Eyring et al., 2021), the best estimates and likely ranges for attributable warming expressed in terms of GMST were assessed to be equal to those for GSAT, which means that the AR6 attributable warming assessment does not distinguish between GMST and GSAT. As such, while WGI Chap. 3 (Eyring et al., 2021) treated estimates of attributable warming in GSAT and GMST from the literature together without any rescaling, we note that climate-model-based estimates of attributable warming in GSAT are expected to be systematically higher than corresponding estimates of attributable warming in GMST (see e.g. Cowtan et al., 2015; Richardson et al., 2018; Beusch et al., 2020; Gillett et al., 2021). Therefore, given an opportunity to update these analyses from AR6, it is more consistent and more comparable with observations of GMST to report attributable changes in GMST using all three methods (described in Sect. S7). The SR1.5 assessment of attributable warming was given in terms of GMST, which is continued here. Therefore, in line with Sect. 7, AR6 WGI, and SR1.5, we adopt GMST as the estimate of global surface temperature. Findings are presented in Figs. S7, S9 and S9 and Tables S4 and S5.

S8.2 Methods to estimate human-induced warming

Both SR1.5 and AR6 drew on evidence from a range of literature for their assessments of human-induced warming, before selecting results from a smaller subset to produce a quantified estimate. While both the SR1.5 and AR6 assessments used the latest Global Warming Index (GWI) results (Haustein et al., 2017), AR6 also incorporated results from two other methods, regularised optimal fingerprinting (ROF) (as in Gillett et al., 2021) and kriging for climate change (KCC) (as in Ribes et al., 2021). In AR6, all three methods gave results consistent not only with each other but also results from AR6 WGI Chap. 7 (see WGI Chap. 7 Supplementary Material (Smith et al., 2021b), Fig. 3.8 of AR6 WGI Chap. 3 (Eyring et al., 2021), and Figs. S7, S8 and S9). Note that the results from Chap. 7 were not included in the AR6 WGI final calculation because they were not statistically independent of other methods. Of the methods used, two (Gillett et al., 2021; Ribes et al., 2021) relied on CMIP6 DAMIP (Gillett et al., 2016) simulations which ended in 2020 and hence require modifications to update to the most recent years. The other two methods (Haustein et al., 2017; Smith et al., 2021b) are fully updatable and can also be made consistent with other aspects of the AR6 assessment and methods. The three methods used in the final assessment of contributions to warming in AR6 are used again with revisions for this annual update and are presented here along with any updates to their approaches.

S8.2.1 Global Warming Index

Introduced in Otto et al. (2015), and refined with full uncertainty assessment in Haustein et al. (2017), the Global Warming Index (GWI) quantifies anthropogenic warming by using an established “multi-fingerprinting” approach to decompose total warming into its various components; preliminary anthropogenic and natural warming time series are first estimated from radiative forcings, and a multivariate linear regression is then taken between these preliminary GMST contributions and observed GMST, with the best fit providing the attributed anthropogenic and natural contributions to warming. As such, the GWI attribution method is directly tied to observations and therefore the resulting central estimate for human-induced warming has a relatively small dependence on the size of the uncertainties in climate sensitivity and forcing.

Substantive annual updates to the GWI assessment depend on annual updates for effective radiative forcings (ERFs) and observed temperature (GMST), both of which are provided as a part of this update (Sects. 5 and 7 respectively). The remaining inputs to the GWI assessment are updated at the less-frequent CMIP cadence; however, these contributions only weakly influence the GWI results. Further, by recomputing a "historical-only" GWI time series based only on data up to a given year, it can be shown that GWI is relatively insensitive to end-date or short-term fluctuations in observed GMST, minimising potential confusion about the current level of warming, such as the perception of a hiatus or acceleration (see AR6 WGI Chapter 3 Cross-Chapter Box 3.1, Eyring et al., 2021), due to short-term internal variability. This, combined with the conceptual simplicity of the method, makes the GWI a relatively transparent and robust method for attributing anthropogenic warming and well-suited to providing reliable annual updates.

Where the GWI method previously separated warming contributions into two components, "anthropogenic" and "natural", and independently attributed them, this update further separates and independently attributes contributions within the Anthropogenic component, adopting the groupings from AR6: "well-mixed greenhouse gases", "other human forcings" and "natural forcings". The climate response model used to estimate (pre-regression) warming from radiative forcing is updated from the AR5 Impulse Response model (AR5-IR; from AR5 Chapter 8 Supplement (Myhre et al., 2013b)) used in Haustein et al. (2017) to the Finite-amplitude Impulse Response model (FaIR; Leach et al., 2021; Smith et al., 2018b; Millar et al., 2017), which was used in SR1.5 and AR6; climate response uncertainty is included by using around 30 sets of parameters that correspond to FaIR emulating the CMIP6 ensemble, as provided in Leach et al. (2021). The updated historical ERF input to FaIR is given in Sect. 5, with uncertainty accounted for using a representative 1000-member probabilistic ensemble. Observed GMST and its uncertainty are provided by the 200-member ensemble of the annually updated HadCRUT5 (Morice et al., 2021; see Sect. 7). Uncertainty from internal variability is accounted for by using between 100-200 realisations of internal variability sampled from the CMIP6 piControl simulations (Nicholls et al., 2021). Since some CMIP6 models may have unrealistically high decadal variability, our estimates of uncertainty may be conservative (Erying et al., 2021). Here, to partly address this, piControl timeseries are first filtered, removing simulations that drift by more than 0.15 °C per decade or exhibit unrealistic variability amplitudes. The parameters for FaIR (given in Leach et al., 2021) are tuned to GSAT outputs from CMIP6; the outputs from FaIR are not rescaled to account for the difference between GSAT and GMST in the tuning since any rescaling would be immediately and completely regressed out in the next step of the attribution process; this lack of rescaling is additionally broadly consistent with the AR6 assessment which concluded with medium confidence that GSAT and GMST are representative of each other – see Sect. S8.1. In future, FaIR could be re-tuned to GMST estimates from CMIP6 in addition to GSAT outputs to examine potential differences in the response that cannot be accounted for through a linear rescaling, though differences in the final attribution results from such a study are expected to be minimal; the regression onto HadCRUT5 provides the strongest constraint.

Producing the GWI ensemble with ~1 billion members is computationally expensive; therefore an ensemble with ~20 million members is randomly subsampled to obtain results, and repeated three times. Uncertainty converges at this scale, and repeat random samplings at the same scale lead to variation in the results of on the order of 0.01 °C.

Compared to Forster et al. (2024), the GWI calculation remains the same, differing only by (i) using ERFs and observed temperatures updated to 2024, and (ii) averaging results across three random ~20 million member sub-samplings instead of ~6 million member sub-samplings (an increase enabled by computing cluster upgrades).

S8.2.2 Kriging for climate change

The kriging for climate change method was originally introduced by Ribes et al. (2021), and subsequently extended in Qasmi and Ribes (2022), to attribute past warming and constrain temperature projections over the 21st century. This statistical method is very similar to ensemble Kalman filtering or kriging. In the original publication (Ribes et al., 2021), a subset of 22 CMIP6 models was considered. For each of them, a statistical procedure was applied to estimate the warming induced by GHG, ANT (temporal smoothing procedure) or NAT (using an Energy Balance Model) forcings, respectively. This subset of models was subsequently used to form an a priori distribution (in a Bayesian sense) of past attributable warming. Then the posterior distribution of past attributable warming given observations was derived. This application was based on HadCRUT4-CW GMST observations (Cowtan and Way, 2014), inflated by 6% to account for the assessment at that time of stronger warming of GSAT relative to GMST.

Results from this calculation were quoted in Eyring et al. (2021). The update made here uses the same subset of 22 CMIP6 models. However, HadCRUT5 observations are used, instead of previous datasets, over an extended 1850-2024 period. Consistent with the AR6 assessment about GMST to GSAT warming ratio, no scaling correction is applied; i.e. the global mean value from HadCRUT5 is assumed to be representative of GSAT changes (see Sect. S8.1). As it relies on available CMIP6 simulations, this update assumes that the world has followed a SSP2-4.5 pathway since 2015. Emissions in the SSP scenarios are similar in the period up until 2024 and close to those which have occurred (e.g. Chen et al., 2021); therefore this is a reasonable approximation. Future updates with this method will incorporate new observations. In parallel, we will try to replace the CMIP6 models by emulators, thus allowing the latest available estimates of radiative forcings to be considered, instead of the SSP2-4.5 scenario.

S8.2.3 Regularized optimal fingerprinting

Optimal fingerprinting is the name given to optimal regression-based approaches to attribution, in which observed anomalies are regressed onto the simulated response to individual forcings from climate models, with the regression coefficients used to infer attributable contributions to observed changes (e.g. Allen and Stott, 2003; Eyring et al., 2021). Ribes et al. (2013) proposed an improved version of the standard total least squares regression, known as regularised optimal fingerprinting, which exhibited improved accuracy in perfect model tests. Gillett et al. (2021) applied this approach to regress observed 5-year mean observed GMST onto the simulated response to individual forcings from the DAMIP simulations (Gillett et al., 2016) of 13 CMIP6 models. In order to ensure a like-for-like comparison, Gillett et al. (2021) regressed observations of GMST, derived from gridded non-infilled near-surface air temperature over land and sea ice, and sea surface temperature over oceans, onto GMST derived from CMIP6 model output in the same way (Cowtan et al., 2015). However, since globally complete GSAT is usually used in the climate impact literature which served as a basis for global warming goals, Gillett et al. (2021) used regression coefficients to infer attributable warming in globally complete GSAT.

Gillett et al. (2021) used CMIP6 DAMIP simulations which generally finished in 2020 and therefore cannot directly be used to infer attributable warming in subsequent years. However, some modelling centres ran single-forcing DAMIP simulations into the future under the SSP2-4.5 scenario (Gillett et al., 2016). Data from concatenated historical and ssp245, hist-nat and ssp245-nat, and hist-GHG and ssp245-GHG were taken from CanESM5 (50, 10, 10), IPSL-CM6A-LR (11, 10, 6) and MIROC6 (3, 50, 50), where numbers in brackets indicate the respective ensemble sizes. Our approach assumes that observed drivers have evolved as in the SSP2-4.5 scenario over the period since 2015, which is a reasonable assumption to the present (e.g. Chen et al., 2021). As in Gillett et al. (2021), internal variability was estimated from intra-ensemble anomalies. Whereas the Gillett et al. (2021) results assessed by Eyring et al. (2021) were based on HadCRUT4, this dataset is no longer being updated, and therefore we use the non-infilled version of HadCRUT5 here (Morice et al., 2021). As shown by Gillett et al. (2021), using HadCRUT5 in place of HadCRUT4 results in a 7% increase in the best estimate of anthropogenic warming for 2010-2019. Gillett et al. (2021) regressed 34 5-year means of GMST over the period 1850-2019 onto simulated GMST over the same period. Here we extend the analysis using 35 5-year means, with the latter based on observations from January 2020 to December 2024 and the model output masked in the same way. In order to be consistent with the Global Warming Index and kriging for climate change approaches described above, and for comparison with GMST observations, we primarily report attributable warming in globally complete GMST here, rather than GSAT (see Sect. S8.1). Calculated anthropogenic warming in GSAT in 2010-2019 computed using HadCRUT5 with this approach of 1.16 (1.04-1.29) °C can be compared with the same quantity reported in Gillett et al. (2021) (their Supplementary Table 1) of 1.18 (1.09-1.27) °C, indicating good consistency.

The method described above is easily updatable into the future using the same set of simulations, simply by updating observations to a later date and masking model output accordingly. As in the KCC method, a caveat to this approach is that it relies on SSP2-4.5 simulations from which actual anthropogenic forcing might be expected to gradually diverge and from which actual natural forcing could rapidly diverge, for example, were a major volcanic eruption to occur.

Table S4 Estimates of global mean surface air temperature (GSAT) warming attributable to multiple influences (in °C) relative to the 1850–1900 baseline period. Values are given as the median, with the 5-95 percentile range in brackets, provided to 0.01°C precision. GSAT results here are only provided for regularised optimal fingerprinting (ROF) because the GSAT results for the other attribution methods (the Global Warming Index (GWI) and kriging for climate change (KCC)) are identical to the GMST results for those methods.

variable	**2010-2019 (decade average)**	**2014-2023 (decade average)**	**2017 (trend-based)**	**2023 (trend-based)**
Human-induced	1.18 (1.05 to 1.32)	1.35 (1.19 to 1.50)	1.22 (1.09 to 1.36)	1.51 (1.33 to 1.69)
Well-mixed greenhouse gases	1.46 (1.25 to 1.68)	1.60 (1.37 to 1.84)	1.51 (1.29 to 1.74)	1.72 (1.47 to 1.98)
Other human forcings	-0.26 (-0.46 to -0.07)	-0.25 (-0.44 to -0.06)	-0.27 (-0.48 to -0.07)	-0.23 (-0.41 to -0.05)
Natural	0.02 (-0.02 to 0.05)	0.01 (-0.03 to 0.05)	0.02 (-0.02 to 0.05)	0.01 (-0.04 to 0.05)

S8.3 Results from each Attribution Method

Results for each attribution method, including headline results and timeseries, are available in csv form in the Climate Indicator repository: https://github.com/ClimateIndicator/anthropogenic-warming-assessment/.

Table S5 Estimates of global mean surface temperature (GMST) warming attributable to multiple influences (in °C) relative to the 1850–1900 baseline period, provided for each warming attribution method and the overall multi-method assessment. Values for individual attribution methods are given as the median, with the 5-95 percentile range in brackets, provided to 0.01 °C precision. Values for the assessment are calculated as defined in Sect. S8.4 and given as best estimates with likely ranges in brackets.

Variable	Method	2010-2019 (decade average)	2015-2024 (decade average)	2017 (single year)	2024 (single year)	2017 (trend-based)	2024 (trend-based)
Human-induced	*GWI*	1.07 (0.95 to 1.17)	1.19 (1.07 to 1.30)	1.13 (1.01 to 1.24)	1.30 (1.16 to 1.43)	1.11 (1.00 to 1.22)	1.31 (1.17 to 1.43)
	KCC	1.06 (0.93 to 1.19)	1.20 (1.05 to 1.34)	1.13 (0.99 to 1.26)	1.32 (1.16 to 1.48)	1.12 (0.98 to 1.25)	1.32 (1.16 to 1.47)
	ROF	1.13 (1.00 to 1.25)	1.28 (1.13 to 1.43)	1.20 (1.04 to 1.35)	1.50 (1.19 to 1.80)	1.16 (1.03 to 1.30)	1.44 (1.27 to 1.61)
	Assessment	1.09 (0.9 to 1.3)	1.22 (1.0 to 1.5)	1.15 (0.9 to 1.4)	1.37 (1.1 to 1.8)	1.13 (0.9 to 1.3)	1.36 (1.1 to 1.7)
Well-mixed greenhouse gases	*GWI*	1.29 (1.04 to 1.54)	1.39 (1.12 to 1.66)	1.34 (1.08 to 1.60)	1.48 (1.20 to 1.78)	1.33 (1.07 to 1.60)	1.48 (1.19 to 1.77)
	KCC	1.50 (1.17 to 1.80)	1.61 (1.25 to 1.95)	1.56 (1.21 to 1.88)	1.72 (1.33 to 2.08)	1.56 (1.21 to 1.88)	1.72 (1.33 to 2.08)
	ROF	1.41 (1.20 to 1.61)	1.53 (1.31 to 1.76)	1.47 (1.24 to 1.69)	1.66 (1.41 to 1.92)	1.45 (1.24 to 1.67)	1.65 (1.41 to 1.89)
	Assessment	1.40 (1.0 to 1.9)	1.51 (1.1 to 2.0)	1.45 (1.0 to 1.9)	1.62 (1.1 to 2.1)	1.45 (1.0 to 1.9)	1.62 (1.1 to 2.1)
Other human forcings	*GWI*	-0.22 (-0.46 to -0.00)	-0.19 (-0.44 to 0.02)	-0.20 (-0.45 to 0.01)	-0.17 (-0.46 to 0.04)	-0.22 (-0.46 to 0.01)	-0.17 (-0.43 to 0.05)
	KCC	-0.43 (-0.72 to -0.14)	-0.42 (-0.72 to -0.11)	-0.43 (-0.72 to -0.13)	-0.40 (-0.71 to -0.08)	-0.43 (-0.72 to -0.13)	-0.40 (-0.72 to -0.08)
	ROF	-0.26 (-0.45 to -0.07)	-0.24 (-0.43 to -0.06)	-0.25 (-0.46 to -0.05)	-0.19 (-0.42 to 0.04)	-0.27 (-0.47 to -0.07)	-0.22 (-0.40 to -0.05)
	Assessment	-0.30 (-0.8 to 0.0)	-0.28 (-0.8 to 0.1)	-0.29 (-0.8 to 0.1)	-0.25 (-0.8 to 0.1)	-0.31 (-0.8 to 0.1)	-0.26 (-0.8 to 0.1)
Natural	*GWI*	0.08 (0.02 to 0.13)	0.08 (0.02 to 0.14)	0.08 (0.02 to 0.14)	0.09 (0.02 to 0.16)	0.08 (0.02 to 0.14)	0.08 (0.02 to 0.14)
	KCC	0.06 (0.04 to 0.08)	0.05 (0.04 to 0.07)	0.06 (0.04 to 0.08)	0.04 (0.03 to 0.06)	0.06 (0.04 to 0.08)	0.04 (0.03 to 0.06)
	ROF	0.02 (-0.02 to 0.05)	0.01 (-0.03 to 0.05)	0.01 (-0.03 to 0.05)	0.00 (-0.04 to 0.05)	0.02 (-0.02 to 0.05)	0.01 (-0.04 to 0.05)
	Assessment	0.05 (-0.1 to 0.2)	0.05 (-0.1 to 0.2)	0.05 (-0.1 to 0.2)	0.04 (-0.1 to 0.2)	0.05 (-0.1 to 0.2)	0.04 (-0.1 to 0.2)

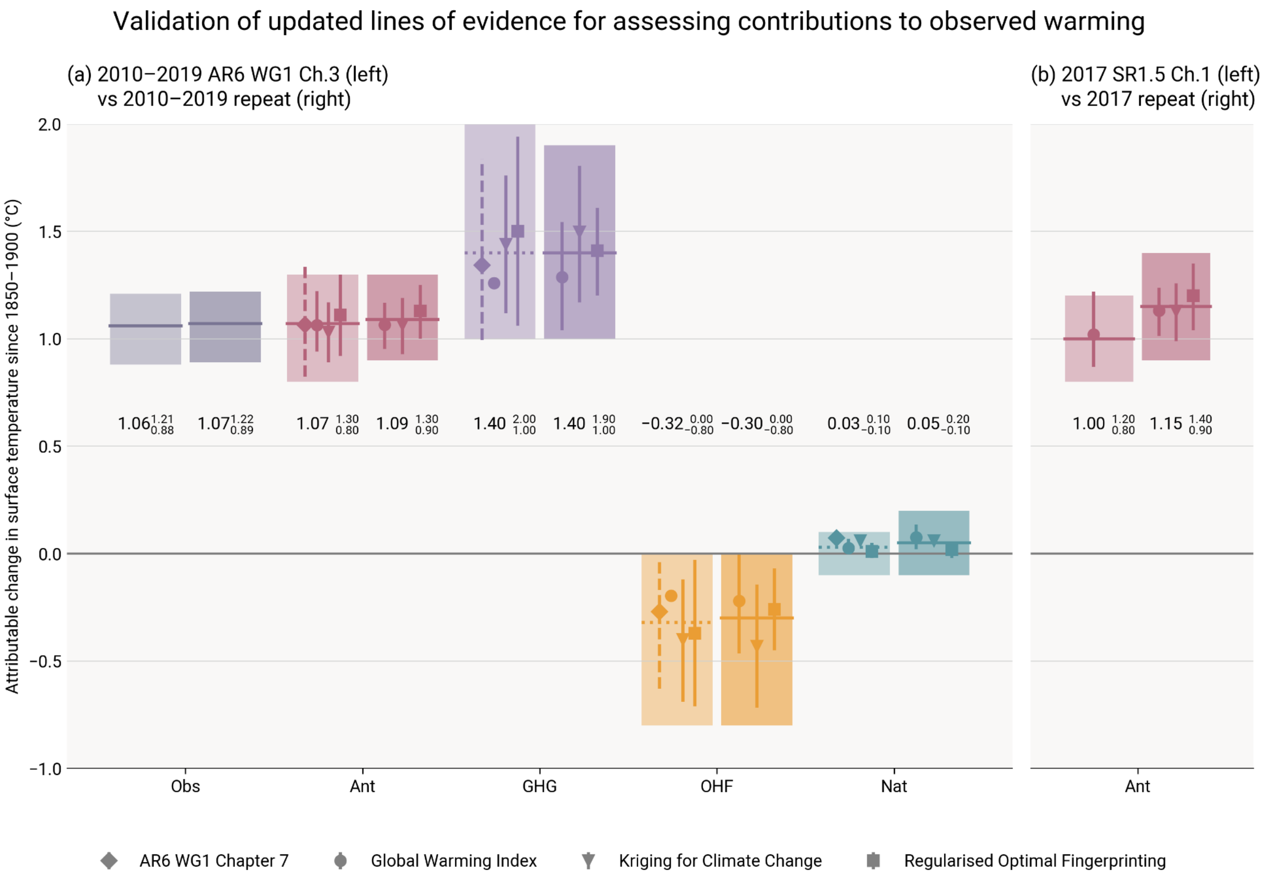

Figure S7 Assessed contributions to observed warming and supporting lines of evidence; see AR6 WG1 Fig. 3.8. The shaded bands show the assessed *likely* ranges of temperature change, relative to the 1850-1900 baseline, attributable to total anthropogenic influence (Ant), well-mixed greenhouse gases (GHGs), other human forcings (OHFs), and natural forcings (Nat). The left of each pair of bands depicts the results quoted from AR6, and the right of each pair of bands depicts a repeat calculation for the same period as the IPCC assessment, using the revised datasets and methods, to validate the updated assessment of attributable warming. Panel (a) presents decade-average warming as used in AR6, with results quoted from AR6 WGI Chapter 3 on the left and the repeat assessment on the right. The solid horizontal bar in each band shows the best estimate for each warming component; if no best estimate was provided, it was retrospectively calculated using the AR6 method and depicted using a horizontal dotted line to facilitate comparison. In AR6, Global Warming Index results were reported as GMST, kriging for climate change results were calculated as GMST and scaled by 1.06 for reporting as GSAT, and regularised optimal fingerprinting was reported as GSAT; for the repeat, all methods are reported in terms of GMST (see Sect. S8.1 for discussion). Panel (b) presents single-year warming as used in SR1.5, with results quoted from SR1.5 Chapter 1 on the left (which was based only on the Global Warming Index) and the repeat assessment on the right, which now includes all of the attribution methods and the multi-method assessment approach used in AR6, as discussed in Sect. S8.4. Both bars are reported in GMST. No assessment was provided for components other than Ant in SR1.5.

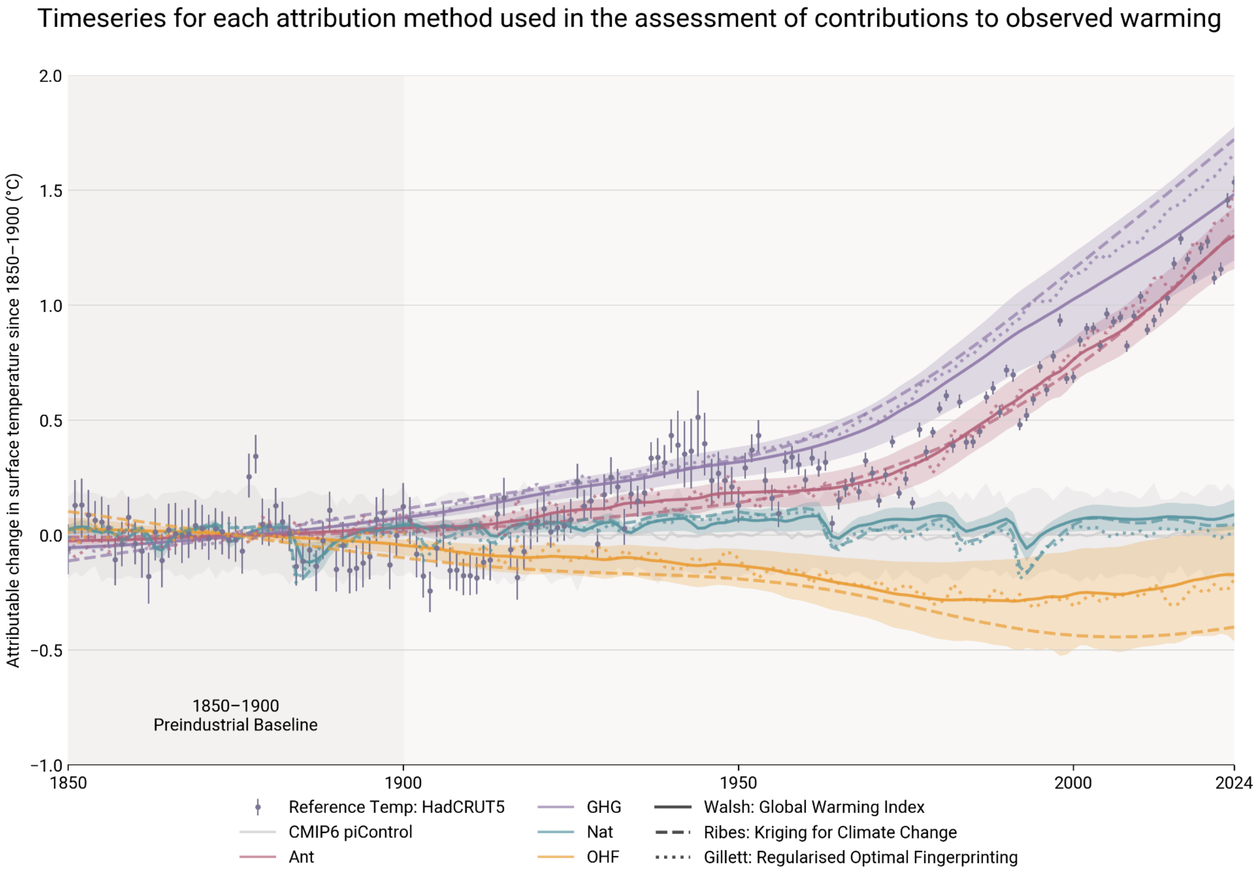

Figure S8 Time series for each attribution method used in the updated assessment of warming contributions, expressed in terms of global mean surface temperature (GMST). Coloured plumes correspond to warming contributions broken down by natural forcings (Nat), well-mixed greenhouse gases (GHGs) and other human forcings (OHFs). Total human-induced warming (Ant) is therefore the sum of contributions from GHG and OHF. The plume range is given by the 5-95% range of the Global Warming Index (GWI), with the GWI best estimate given by the solid lines. The dashed line presents the best estimate from the kriging for climate change (KCC) method, and the dotted line presents the best estimate from the regularised optimal fingerprinting (ROF) method. GWI and KCC are given as annual values based on infilled GMST from HadCRUT5; ROF is given as annual values of globally complete GMST. The CMIP6 pre-industrial control (piControl) simulations are used as a proxy for multiple samplings of internal variability and are used to account for attribution uncertainty resulting from internal variability in the GWI method (see Sect. S8.2.1).

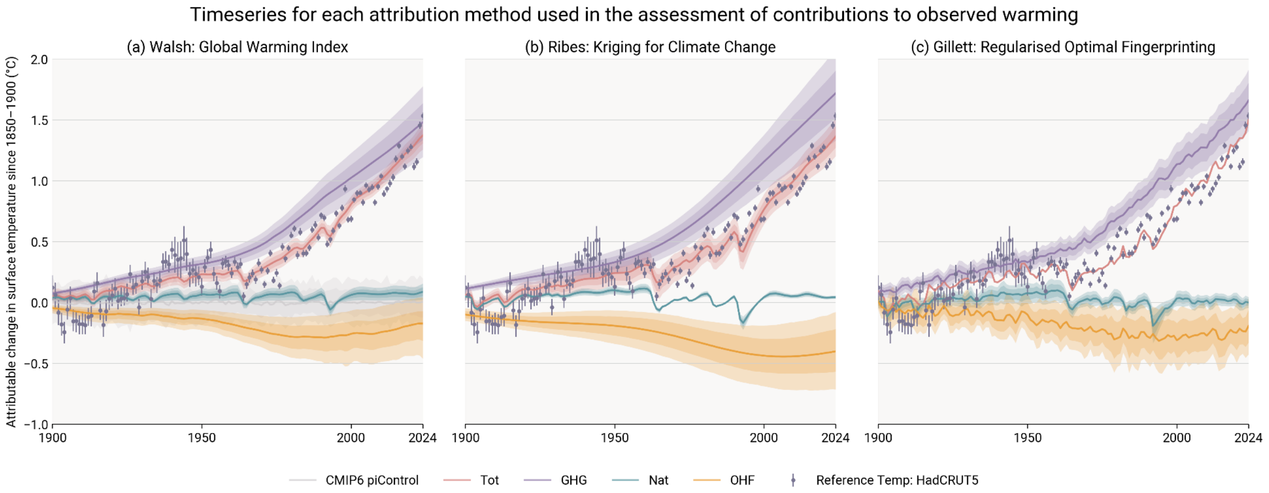

Figure S9 Time series for each attribution method used in the updated assessment of warming contributions, expressed in terms of global mean surface temperature (GMST). Coloured plumes are given for both 17-83% and 5-95% ranges and correspond to warming contributions to observed warming broken down by natural forcings (Nat), well-mixed greenhouse gases (GHGs) and other human forcings (OHFs). Total warming (Tot) is the total attributable warming and therefore the sum of contributions from GHG, OHF and Nat. Observation data from (infilled) HadCRUT5 are presented with 9-95% uncertainty bars. Panel (a) presents results from the Global Warming Index method (Sect. S8.2.1); the CMIP6 pre-industrial control (piControl) simulations are used as a proxy for multiple samplings of internal variability and used to account for uncertainty in the attribution resulting from internal variability (see Sect. S8.2.1). Panel (b) presents results from the kriging for climate change methods (Sect. S8.2.2). Panel (c) presents results from regularised optimal fingerprinting (Sect. S8.2.3), with the time series for Tot being approximated by the sum of the Ant and Nat medians; note that this is different from GWI and KCC, where Tot is a directly attributed quantity.

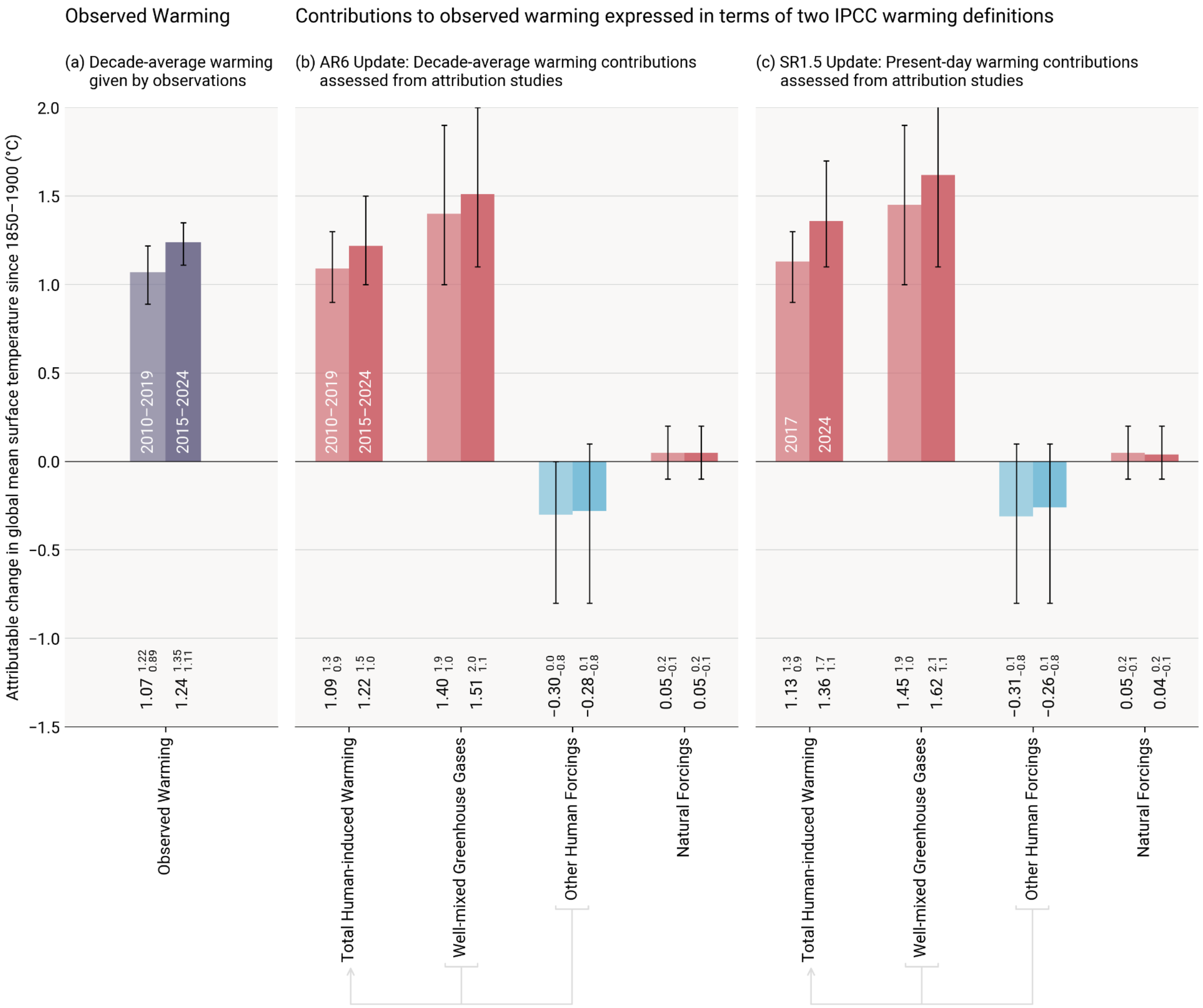

Figure S10 A repeat of Fig. 9 depicting changes to the assessed levels of warming since the sixth assessment cycle. Updated assessed contributions to observed warming relative to 1850–1900; see AR6 WGI SPM.2. Results for all time periods in this figure are calculated using updated datasets and methods. To show how these updates have affected the previous assessments, the 2010–2019 average assessed results repeat the AR6 2010–2019 assessment, and the 2017 assessed results repeat the SR1.5 2017 assessment. The 2015–2024 average and 2024 results are this year's updated assessments for AR6 and SR1.5, respectively. For each double bar, the lighter and darker shading refers to the earlier and later period, respectively. Panel (a) shows updated observed global warming from Sect. 7, expressed as total global mean surface temperature (GMST), due to both anthropogenic and natural influences. Whiskers give the "*very likely*" range. Panels (b) and (c) show updated assessed contributions to warming, expressed as global mean surface temperature (GMST), from natural forcings and total human-induced forcings, which in turn consist of contributions from well-mixed greenhouse gases and other human forcings . Whiskers give the "*likely*" range.

S8.4 Updated IPCC assessment approach of attributed global warming

S8.4.1 Updated estimate using the AR6 WGI methodology

Factoring in results from each of the three attribution methods (see Sect. S8.2), AR6 WGI Chap. 3 (Eyring et al., 2021) defined the *likely* range for each warming component as the smallest 0.1 °C precision range that enveloped the 5th to 95th percentile ranges of each method. In addition, a best estimate was provided for the human-induced (Ant) warming component, calculated as the mean of the 50th percentile values for each method. Best estimates were not provided in AR6 for the other components (well-mixed greenhouse gases (GHGs), other human forcings (OHFs) and natural forcings (Nat)), with their values in AR6 WGI Fig. SPM.2(b) simply being given as the midpoint between the lower and upper bound of the *likely* range and therefore not directly comparable with the central values given for human-induced and observed warming. In order to make a meaningful and consistent comparison, and provide insight into interannual changes, an improvement is made in this update: the multi-method-mean best-estimate approach is extended for all warming components.

Note that in IPCC assessments, *likely* statements typically correspond to 66–100% probability, whereas *very likely* statements correspond to 90–100% probability. Despite deriving the overall multi-method uncertainty ranges from the 5-95th percentile ranges for each method, the overall uncertainty was conservatively assessed in AR6 to be *likely* rather than *very likely,* which noted that the methods may "underestimate the importance of the structural limitations of climate models, which probably do not represent all possible sources of internal variability; use too simple climate models, which may underestimate the role of internal variability; or underestimate model uncertainty, especially when using model ensembles of limited size and inter-dependent models, for example through common errors in forcings across models" (Eyring et al., 2021). We maintain this choice of *likely* in these updates. The *likely* confidence of the AR6 assessment is also consistent with the *likely* confidence given in SR1.5 assessment - see Supplement Sect. S8.4.2.

S8.4.2 Updated estimate using the SR1.5 methodology applied to the AR6 WGI datasets

While a variety of literature was drawn upon for the assessment of human-induced warming in SR1.5 Chap. 1 (Allen et al., 2018), only one method, the Global Warming Index (GWI), was used to provide a quantitative assessment of the 2017, "current", level of human-induced warming. The latest results for this method were provided by Haustein et al. (2017), who gave a central estimate for human-induced warming in 2017 of 1.01 °C with a 5 %–95 % range of (0.87 to 1.22 °C). SR1.5 then accounted for methodological uncertainty by rounding this value to 0.1 °C precision for its final assessment of 1.0 °C and assessing the 0.8 to 1.2 °C range as a *likely* range. No assessment of the contributions from other components was provided due to limitations in the GWI approach at the time.

While it is possible to continue the SR1.5 assessment approach of using a single method (GWI) rounded to 0.1 °C precision, for the purpose of providing annual updates this is insufficient; (i) 0.1 °C precision is too coarse to capture meaningful inter-annual changes to the level of current warming, (ii) using different selections of methods prevents meaningful comparison between the results for decadal mean and current single-year warming calculations, and (iii) using the mean of multiple methods increases the robustness of the results. These points are simultaneously addressed in this update by adopting the latest multi-method assessment approach, as established in WGI AR6, for both the AR6 decadal mean warming update and the SR1.5 current single-year warming update. Further, where SR1.5 only provided an assessment for human-induced warming, updates in available attribution methods since SR1.5 mean that it is now also possible to provide a fully consistent assessment for all warming components. As with the attribution assessment in SR1.5, this update reports values in Table 6b of the main paper for the current single-year attributable warming calculated as a simple annual-mean (as discussed in Sect. 8.1), with a comparison to results for the current single-year attributable warming calculated using the SR1.5 trend-based definition also provided in Sect. 8.3.

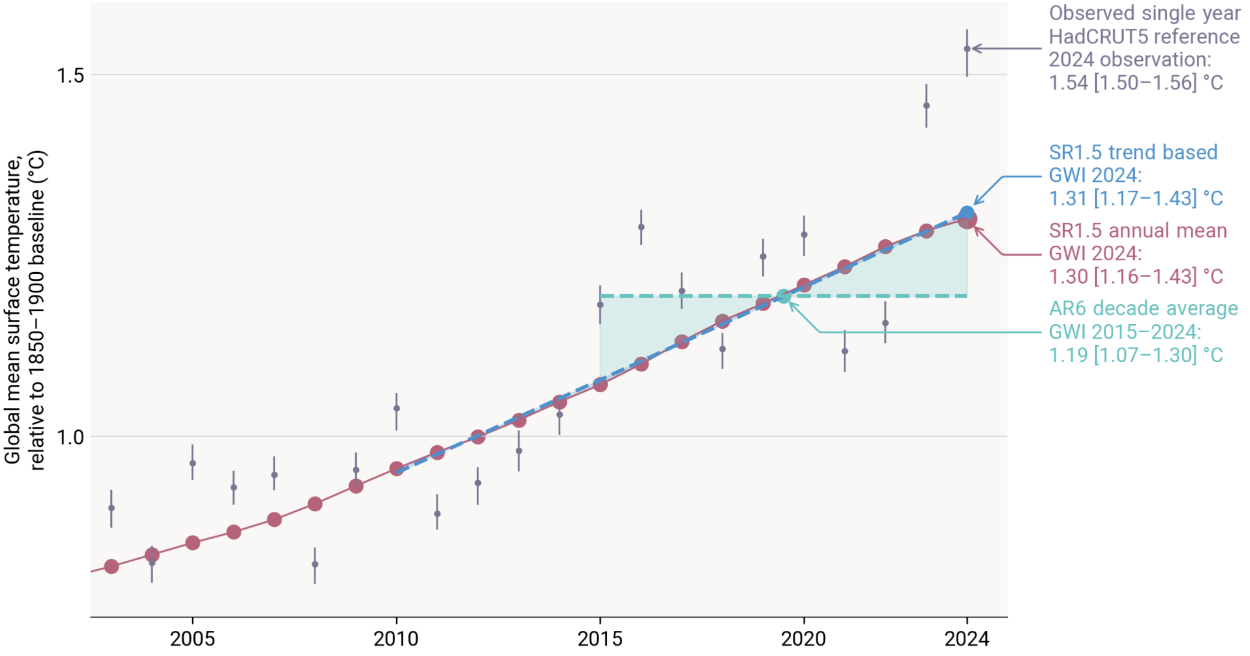

Figure S11 Anthropogenic warming period definitions adopted in the IPCC sixth assessment cycle. A single sampled time series of anthropogenic warming is shown in red (in this case from the GWI method – see Sect. S8.2.1). Annual-mean warming is given by the annual values of the GWI time series. The AR6 decade-average warming is given by the average of the 10 most recent annual-mean anthropogenic warming values; this is depicted by the dashed green line with shading between this and the red annual-mean values. The decade-average value for 2015–2023 is given by the green dot. SR1.5 trend-based warming is given by the end point of the linear trend line through the 15 most recent annual-mean anthropogenic warming values; this is depicted by the dashed blue line with shading between this and the red annual-mean values; the trend-based value for 2024 is given by the blue dot. Reference observations of GMST are provided from HadCRUT5, with 5 %–95 % uncertainty range. In practice, the annual-mean, trend-based, and decade-average calculations are applied at the level of the individual ensemble members for each of the three attribution methods; percentiles of those ensemble results provide central estimates and uncertainty ranges for each method, and the multi-method assessment combines those into the final assessment results with uncertainty (as described in Sect. S8.4). For reference, the GWI results for 2024 (provided in Sect. 8.3) are annotated in the figure.

S8.5 Rate of human-induced warming

S8.5.1 SR1.5 and AR6 definitions of warming rate

As in previous years' assessments we use recent IPCC assessments' definitions of anthropogenic warming rate. These follow two approaches, both of which rely to some extent on expert judgment. In SR1.5 a number of separate studies were considered, with each study defining the rate of warming in a separate way. The SR1.5 assessment concluded that the rate of increase of anthropogenic warming in 2017 was 0.2 °C per decade, with a likely range spanning 0.1 °C to 0.3 °C per decade. In AR6 WGI the rate of anthropogenic warming utilised three methods (GWI, KCC, ROF; see definitions in Section S8.2) with the rate defined as the linear trend in the preceding decade of attributed anthropogenic warming. While best-estimate trends reported in AR6 were all higher than in SR1.5's assessment, Eyring et al. (2021) concluded that there was insufficient evidence to change the SR1.5 assessed anthropogenic warming trend in the AR6 WGI report, which therefore remained at 0.2 °C per decade (with a likely range spanning 0.1 °C to 0.3 °C per decade).

S8.5.2 Methods

Following AR6's definition, the rate of warming is defined here as the rolling 10-year linear trend in attributed anthropogenic warming, calculated using ordinary least-squares linear regression. Note that, as with the level of anthropogenic warming, this decadal approach means the rate of warming in a given year is the trend centred on the preceding decade (i.e. it is 5 years out of date). Each of the three attribution methods used to calculate the level of warming are again used here to estimate separate anthropogenic warming rates.

Note that only the GWI methodology relies on the updated historical forcing timeseries presented in Sect. 5, with the other two methods (ROF and KCC) relying on CMIP6 SSP2-4.5 simulations, which are increasingly out of date (see Sect. S8.2). Very recent changes in anthropogenic forcing, for example desulphurisation of shipping fuels or the impact of COVID-19, may therefore not be captured fully in the decade-average trend. Further, the anthropogenic forcing record used for attributing warming contains small contributions from biomass burning in the natural environment, because of difficulty separating this in estimates of anthropogenic aerosol emissions. It is not expected that either of these effects substantially bias the globally-averaged rate of warming estimated here.

S8.5.3 Results

Individual warming rate attributions are revised upwards slightly from previous years (see Table 7 in main text). GWI and KCC methodologies are increased by 0.01 °C/decade for the decade 2015-2024, while ROF is increased by 0.04 °C/decade. This increase in the ROF method's rate principally reflects the fact that the methodology, based on a linear regression of CMIP ensemble member's historical (plus SSP scenario projection to present day) warming onto observed GMST anomaly, is strongly influenced by residual internal variability that remains in the anthropogenic warming signal due to the limitations in size of the CMIP ensemble, particularly given that the number of CMIP ensemble members which project ensemble members forward to 2024 is reduced compared to those running the full historical experiment.

Table S6 Estimates of the rate of anthropogenic warming (in °C per decade), provided for each warming attribution method and the overall multi-method assessment. Values for individual attribution methods are calculated as defined in Sect. S8.5 (least squares fit through most recent 10-year period), with best estimates provided as the median, with the 5-95 percentile range in brackets, provided to 0.01 °C precision.

Variable	Method	2010-2019 AR6 Quote	2010-2019 Repeat	2015-2024
Rate of human-induced warming	*GWI*	0.23 [0.19 to 0.35]	0.25 [0.19 to 0.30] GMST	0.25 [0.20 to 0.30] GMST
	KCC	0.23 [0.19 to 0.29]	0.26 [0.24 to 0.32] GMST	0.27 [0.24 to 0.32] GMST
	ROF	0.35 [0.30 to 0.41]	0.27 [0.17 to 0.38] GMST	0.42 [0.25 to 0.59] GMST
	Assessment	0.2 [0.1 to 0.3]	0.26 [0.2 to 0.4]	0.27 [0.2 to 0.4]

S9. Remaining carbon budget

The remaining carbon budget is tabulated below for all decimals between 1.5 °C and 2 °C. In Table S7 we present results directly comparable to Table 8 of the main paper for an expanded range of probabilities and temperature limits. In Table S8 we average the non-CO_2 impacts as estimated by MAGICC (as in other tables) and the simple climate model FaIR. We also include an uncertainty of 0.19 °C in the post-net zero warming (ZEC) in Table S8. This corresponds to the "default update" in Lamboll et al. (2023), using the updated values for recent temperatures and emissions.

Table S7 remaining carbon budgets. This is an expanded version of Table 8 in the main paper.

Temperature (°C)	Estimated remaining carbon budgets from the beginning of 2025 base year ($GtCO_2$)						
Avoidance probability (TCRE uncertainty only):	10%	17%	33%	50%	67%	83%	90%

1.5	460	320	200	130	80	30	10
1.6	820	620	420	310	240	160	130
1.7	1190	910	640	490	390	290	250
1.8	1550	1200	860	680	550	430	370
1.9	1920	1500	1090	860	710	560	480
2	2290	1790	1310	1050	870	690	600

Table S8 remaining carbon budgets, including uncertainty in ZEC and averaging results from MAGICC and FaIR for non-CO_2 warming.

Temperature (°C)	Estimated remaining carbon budgets from the beginning of 2025 base year ($GtCO_2$)						
Avoidance probability (TCRE and ZEC uncertainty):	10%	17%	33%	50%	67%	83%	90%
1.5	980	710	400	180	10	-220	-370
1.6	1280	950	600	360	180	-50	-180
1.7	1580	1210	800	550	350	120	-20
1.8	1910	1470	1010	730	510	280	140
1.9	2240	1740	1220	910	680	430	290
2	2570	2010	1430	1090	840	580	440

Estimating the remaining carbon budget (RCB) requires an estimate of future non-CO_2 warming. The latter estimate is derived from the emissions trajectories as modelled by internally consistent emissions scenarios. While RCB estimates are for CO_2 emissions only, the consideration of non-CO_2 warming implies that assumptions are also made about reductions in other anthropogenic forcers (Rogelj and Lamboll, 2024). These reductions have to be kept in mind, as a shortfall in non-CO_2 greenhouse gas emissions would result in a smaller RCB estimate. For instance, as reported in Rogelj and Lamboll (2024), the estimate of RCBs consistent with limiting warming to 1.5 °C assumes a median reduction in CH_4 emissions between 2020 and 2050 of 51% (while the interquartile range across available scenarios is 47–60%), a 22% reduction between 2020 and 2050 in N_2O emissions (interquartile range: 7–35%), and a 78% reduction between 2020 and 2050 in SO_2 emissions (interquartile range: 74–78%). Assumed reductions consistent with other levels of warming are reproduced from Rogelj and Lamboll (2024) and provided in Table S9. The estimates reported in Table 8 of the main paper are based on the median non-CO_2 emission reductions. Falling short of achieving the assumed non-CO_2 greenhouse gas emissions reductions would further reduce the RCB. Sulphur dioxide emissions are more tightly co-controlled with CO_2 reduction because of the phase-out of unabated fossil fuel combustion and air pollution control measures (Rogelj et al., 2014a, 2014b). A shortfall in their reductions would therefore be less conceivable in a net-zero CO_2 world.

Table S9 Non-CO_2 reductions implied in Remaining Carbon Budget (RCB) estimates, adapted from Rogelj and Lamboll (2024). Values represent the changes in non-CO_2 emissions between 2020 and 2050 consistent with the RCB estimates for 1.5°C, 1.7°C and 2.0°C. The median changes are the default and marked in light blue. Any deviation from this median assumption results in an increase or decrease of the RCB estimate.

Temperature level for which RCB was estimated	**Percentile**	**Implied non-CO_2 change between 2020 and 2050 [%]**		
		CH_4	**N_2O**	**SO_2**
1.5°C	**10th**	-69	-47	-80
	25th	-60	-35	-78
	50th	-51	-22	-78
	75th	-47	-7	-74
	90th	-39	+2	-66
1.7°C	**10th**	-62	-42	-78
	25th	-53	-30	-76
	50th	-44	-18	-73
	75th	-39	-3	-68

	90th	-31	+6	-60
2.0°C	**10th**	-51	-35	-75
	25th	-43	-23	-72
	50th	-34	-11	-66
	75th	-27	+2	-59
	90th	-20	+12	-51

S10. Examples of climate and weather extremes: maximum temperature over land

Land average annual maximum temperature (TXx) - Methods

The choice of datasets for the analysis of land average TXx is based on a trade-off between record length, data availability, near real-time updates, and long-term support. As the indicator averages over all available land grid points, the spatial coverage should be high to obtain a meaningful average, which further limits the choice of datasets. The HadEX3 dataset (Dunn et al., 2020), which is used for Fig. 11.2 in Seneviratne et al. (2021), is static and does not cover years after 2018. We therefore additionally include the Berkeley Earth Surface Temperature dataset (building off Rohde et al., 2013) and the fifth-generation ECMWF atmospheric reanalysis of the global climate (ERA5; Hersbach et al., 2020). Berkeley Earth data currently enable an analysis of annual indices up to 2023, while ERA5 covers the whole of 2024 as it is updated daily with a latency of about 5 d (and the final release occurs after 2–3 months).

For HadEX3, we select the years 1961–2018, to exclude years with insufficient data coverage, and require at least 90 % temporal completeness, thus applying the same criteria as for Fig. 11.2 in Seneviratne et al. (2021). Berkeley Earth provides daily maximum temperatures, and we require more than 99 % data availability for each individual year and grid point, such that years with more than 4 missing days are removed. Based on this criterion, Berkeley Earth covers at least 95 % of the global land area from 1955 onwards. ERA5, on the other hand, has full spatio-temporal coverage by design, and hence the entire currently available period of 1950–2024 is used. The annual maximum temperature is then computed for each grid point, and a global area-weighted average is calculated for all grid points with at least 90 % temporal completeness in the respective available period (1955–2023 and 1961–2018 for Berkeley Earth and HadEX3, while ERA5 is again not affected by this criterion). We thus enforce high data availability to adequately calculate global land averaged TXx across all three datasets, but their coverage is not identical, which introduces minor deviations in the estimated global land averages. The resulting TXx time series are then computed as anomalies with respect to a baseline period of 1961–1990. Note that the Berkeley Earth daily maximum data has been updated, with changes of several °C for individual grid points and days. These changes partially compensate such that the TXx estimates for individual years differ less than 0.1 °C.

To express the TXx as anomalies with respect to 1850–1900, we add an offset to all three datasets. The offset is based on the Berkeley Earth data and is derived from the linear regression of land mean TXx to the annual mean global mean air temperature over the period 1955–2020. The offset is then calculated as the slope of the linear regression times the global mean temperature difference between the reference periods 1850–1900 and 1961–1990 (see Fig. S12). The updated Berkeley Earth data led to a change in offset of 0.01°C compared to Forster et al. (2024).

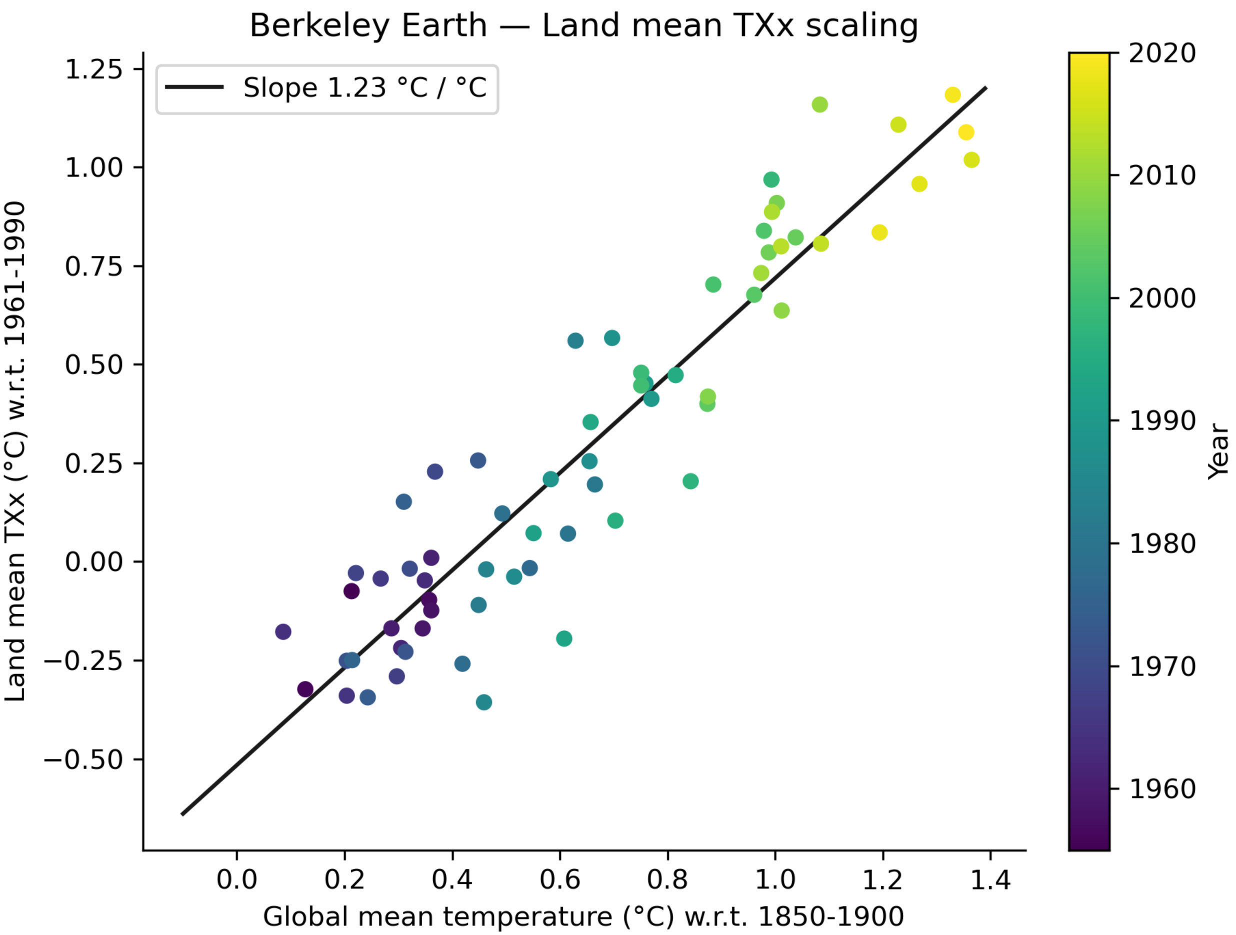

Figure S12 Calculation of relationship between land mean annual maximum temperature (TXx) and global mean temperature. This is used to determine the TXx offset between 1850–1900 and 1961–1990. A linear regression of TXx as a function of global mean temperature from Berkeley Earth is fitted to data from 1955–2020. The TXx offset of 0.51 °C is then obtained by multiplying the slope of the linear regression (1.23 °C / °C) with the global mean temperature difference between 1850–1900 and 1961–1990 (0.42°C).

References

Adusumilli, S., Straneo, F., Hendricks, S., Korosov, A., Lavergne, T., Lawrence, I., Marzeion, B., Otosaka, I., Schweiger, A., Shepherd, A., Slater, D., Slater, T., Timmermanns, M.-L., and Zemp, M.: GCOS EHI 1960-2020 Cryosphere Heat Content, https://doi.org/10.26050/WDCC/GCOS_EHI_1960-2020_CRHC, 2022.

Allen, M. R. and Stott, P. A.: Estimating signal amplitudes in optimal fingerprinting, part I: theory, Climate Dynamics, 21, 477–491, https://doi.org/10.1007/s00382-003-0313-9, 2003.

Allen, M. R., O. P. Dube, W. Solecki, F. Aragón-Durand, W. Cramer, S. Humphreys, M. Kainuma, J. Kala, N. Mahowald, Y. Mulugetta, R. Perez, M. Wairiu, and K. Zickfeld, 2018: Framing and Context. In: Global Warming of 1.5°C. An IPCC Special Report on the impacts of global warming of 1.5°C above pre-industrial levels and related global greenhouse gas emission pathways, in the context of strengthening the global response to the threat of climate change, sustainable development, and efforts to eradicate poverty [Masson-Delmotte, V., P. Zhai, H.-O. Pörtner, D. Roberts, J. Skea, P.R. Shukla, A. Pirani, W. Moufouma-Okia, C. Péan, R. Pidcock, S. Connors, J.B.R. Matthews, Y. Chen, X. Zhou, M.I. Gomis, E. Lonnoy, T. Maycock, M. Tignor, and T. Waterfield (eds.)], Cambridge University Press, Cambridge, UK and New York, NY, USA, 49-92, https://doi.org/10.1017/9781009157940.003, 2018.

Beusch, L., Gudmundsson, L., and Seneviratne, S. I.: Emulating Earth system model temperatures with MESMER: from global mean temperature trajectories to grid-point-level realizations on land, Earth Syst. Dynam., 11, 139–159, https://doi.org/10.5194/esd-11-139-2020, 2020.

Chen, D., M. Rojas, B. H. Samset, K. Cobb, A. Diongue Niang, P. Edwards, S. Emori, S. H. Faria, E. Hawkins, P. Hope, P. Huybrechts, M. Meinshausen, S. K. Mustafa, G.-K. Plattner, and A.-M. Tréguier, 2021: Framing, Context, and Methods. In Climate Change 2021: The Physical Science Basis. Contribution of Working Group I to the Sixth Assessment Report of the Intergovernmental Panel on Climate Change [Masson-Delmotte, V., P. Zhai, A. Pirani, S. L. Connors, C. Péan, S. Berger, N. Caud, Y. Chen, L. Goldfarb, M. I. Gomis, M. Huang, K. Leitzell, E. Lonnoy, J. B. R. Matthews, T. K. Maycock, T. Waterfield, O. Yelekçi, R. Yu, and B. Zhou (eds.)]. Cambridge University Press, Cambridge, United Kingdom and New York, NY, USA, pp. 147–286, https://doi.org/:10.1017/9781009157896.003, 2021.

Cheng, L., Trenberth, K. E., Fasullo, J., Boyer, T., Abraham, J., and Zhu, J.: Improved estimates of ocean heat content from 1960 to 2015, Sci. Adv., 3, e1601545, https://doi.org/10.1126/sciadv.1601545, 2017.

Cowtan, K. and Way, R. G.: Coverage bias in the HadCRUT4 temperature series and its impact on recent temperature trends, Q.J.R. Meteorol. Soc., 140, 1935–1944, https://doi.org/10.1002/qj.2297, 2014.

Cowtan, K., Hausfather, Z., Hawkins, E., Jacobs, P., Mann, M. E., Miller, S. K., Steinman, B. A., Stolpe, M. B., and Way, R. G.: Robust comparison of climate models with observations using blended land air and ocean sea surface temperatures, Geophys. Res. Lett., 42, 6526–6534, https://doi.org/10.1002/2015GL064888, 2015.

Cuesta-Valero, F. J., García-García, A., Beltrami, H., González-Rouco, J. F., and García-Bustamante, E.: Long-term global ground heat flux and continental heat storage from geothermal data, Clim. Past, 17, 451–468, https://doi.org/10.5194/cp-17-451-2021, 2021.

Cuesta-Valero, F. J., Beltrami, H., García-García, A., Krinner, G., Langer, M., MacDougall, A. H., Nitzbon, J., Peng, J., von Schuckmann, K., Seneviratne, S. I., Smith, N., Thiery, W., Vanderkelen, I., and Wu, T.: Continental heat storage: Contributions from ground, inland waters, and permafrost thawing, Earth Syst. Dynam. Discuss. [preprint], https://doi.org/10.5194/esd-2022-32, 2023.

Deng, Z., Ciais, P., Tzompa-Sosa, Z. A., Saunois, M., Qiu, C., Tan, C., Sun, T., Ke, P., Cui, Y., Tanaka, K., Lin, X., Thompson, R. L., Tian, H., Yao, Y., Huang, Y., Lauerwald, R., Jain, A. K., Xu, X., Bastos, A., Sitch, S., Palmer, P. I., Lauvaux, T., d'Aspremont, A., Giron, C., Benoit, A., Poulter, B., Chang, J., Petrescu, A. M. R., Davis, S. J., Liu, Z., Grassi, G., Albergel, C., Tubiello, F. N., Perugini, L., Peters, W., and Chevallier, F.: Comparing national greenhouse gas budgets reported in UNFCCC inventories against atmospheric inversions, Earth Syst. Sci. Data, 14, 1639–1675, https://doi.org/10.5194/essd-14-1639-2022, 2022.

Dessler, A. E., Schoeberl, M. R., Wang, T., Davis, S. M., Rosenlof, K. H., and Vernier, J.-P.: Variations of stratospheric water vapor over the past three decades, J. Geophys. Res.-Atmos., 119, 12588-12598, https://doi.org/10.1002/2014JD021712, 2014.

Dhomse, S. S., Mann, G. W., Antuña Marrero, J. C., Shallcross, S. E., Chipperfield, M. P., Carslaw, K. S., Marshall, L., Abraham, N. L., and Johnson, C. E.: Evaluating the simulated radiative forcings, aerosol properties, and stratospheric warmings from the 1963 Mt Agung, 1982 El Chichón, and 1991 Mt Pinatubo volcanic aerosol clouds, Atmos. Chem. Phys., 20, 13627–13654, https://doi.org/10.5194/acp-20-13627-2020, 2020.

Domingues, C. M., Church, J. A., White, N. J., Gleckler, P. J., Wijffels, S. E., Barker, P. M., and Dunn, J. R.: Improved estimates of upper-ocean warming and multi-decadal sea-level rise, Nature, 453, 1090–1093, https://doi.org/10.1038/nature07080, 2008.

Dunn, R. J. H., Alexander, L. V., Donat,M. G., Zhang, X., Bador, M., Herold, N.,et al. Development of an updated global land in situ-based dataset of temperature and precipitation extremes: HadEX3, J.Geophys. Res.-Atmos.,125, e2019JD032263, https://doi.org/10.1029/2019JD032263R, 2020.

Dutton, G.S., B. D. Hall, S.A. Montzka, J. D. Nance, S. D. Clingan, K. M. Petersen, Combined Atmospheric Chloroflurocarbon-12 Dry Air Mole Fractions from the NOAA GML Halocarbons Sampling Network, 1977-2024, Version: 2024-03-07, https://doi.org/10.15138/PJ63-H440, 2024.

Etminan, M., Myhre, G., Highwood, E. J., and Shine, K. P.: Radiative forcing of carbon dioxide, methane, and nitrous oxide: A significant revision of the methane radiative forcing, Geophys. Res. Lett., 43, 12614-12623, https://doi.org/10.1002/2016GL071930, 2016.

Eyring, V., N. P. Gillett, K.M. Achuta Rao, R. Barimalala, M. Barreiro Parrillo, N. Bellouin, C. Cassou, P. J. Durack, Y. Kosaka, S. McGregor, S. Min, O. Morgenstern, and Y. Sun: Human Influence on the Climate System. In Climate Change 2021: The Physical Science Basis. Contribution of Working Group I to the Sixth Assessment Report of the Intergovernmental

Panel on Climate Change[Masson-Delmotte, V., P. Zhai, A. Pirani, S.L. Connors, C. Péan, S. Berger, N. Caud, Y. Chen, L. Goldfarb, M.I. Gomis, M. Huang, K. Leitzell, E. Lonnoy, J.B.R. Matthews, T.K. Maycock, T. Waterfield, O. Yelekçi, R. Yu, and B. Zhou (eds.)]. Cambridge University Press, Cambridge, United Kingdom and New York, NY, USA, pp. 423–552, http://doi:10.1017/9781009157896.005, 2021.

Forster, P., T. Storelvmo, K. Armour, W. Collins, J.-L. Dufresne, D. Frame, D.J. Lunt, T. Mauritsen, M.D. Palmer, M. Watanabe, M. Wild, and H. Zhang, 2021: The Earth's Energy Budget, Climate Feedbacks, and Climate Sensitivity. In Climate Change 2021: The Physical Science Basis. Contribution of Working Group I to the Sixth Assessment Report of the Intergovernmental Panel on Climate Change [Masson-Delmotte, V., P. Zhai, A. Pirani, S.L. Connors, C. Péan, S. Berger, N. Caud, Y. Chen, L. Goldfarb, M.I. Gomis, M. Huang, K. Leitzell, E. Lonnoy, J.B.R. Matthews, T.K. Maycock, T. Waterfield, O. Yelekçi, R. Yu, and B. Zhou (eds.)]. Cambridge University Press, Cambridge, United Kingdom and New York, NY, USA, pp. 923–1054, https://doi.org/10.1017/9781009157896.009, 2021.

Forster, P. M., Smith, C. J., Walsh, T., Lamb, W. F., Lamboll, R., Hauser, M., Ribes, A., Rosen, D., Gillett, N., Palmer, M. D., Rogelj, J., von Schuckmann, K., Seneviratne, S. I., Trewin, B., Zhang, X., Allen, M., Andrew, R., Birt, A., Borger, A., Boyer, T., Broersma, J. A., Cheng, L., Dentener, F., Friedlingstein, P., Gutiérrez, J. M., Gütschow, J., Hall, B., Ishii, M., Jenkins, S., Lan, X., Lee, J.-Y., Morice, C., Kadow, C., Kennedy, J., Killick, R., Minx, J. C., Naik, V., Peters, G. P., Pirani, A., Pongratz, J., Schleussner, C.-F., Szopa, S., Thorne, P., Rohde, R., Rojas Corradi, M., Schumacher, D., Vose, R., Zickfeld, K., Masson-Delmotte, V., and Zhai, P.: Indicators of Global Climate Change 2022: annual update of large-scale indicators of the state of the climate system and human influence, Earth Syst. Sci. Data, 15, 2295–2327, https://doi.org/10.5194/essd-15-2295-2023, 2023.

Friedlingstein, P., O'Sullivan, M., Jones, M. W., Andrew, R. M., Hauck, J., Landschützer, P., Le Quéré, C., Li, H., Luijkx, I. T., Olsen, A., Peters, G. P., Peters, W., Pongratz, J., Schwingshackl, C., Sitch, S., Canadell, J. G., Ciais, P., Jackson, R. B., Alin, S. R., Arneth, A., Arora, V., Bates, N. R., Becker, M., Bellouin, N., Berghoff, C. F., Bittig, H. C., Bopp, L., Cadule, P., Campbell, K., Chamberlain, M. A., Chandra, N., Chevallier, F., Chini, L. P., Colligan, T., Decayeux, J., Djeutchouang, L. M., Dou, X., Duran Rojas, C., Enyo, K., Evans, W., Fay, A. R., Feely, R. A., Ford, D. J., Foster, A., Gasser, T., Gehlen, M., Gkritzalis, T., Grassi, G., Gregor, L., Gruber, N., Gürses, Ö., Harris, I., Hefner, M., Heinke, J., Hurtt, G. C., Iida, Y., Ilyina, T., Jacobson, A. R., Jain, A. K., Jarníková, T., Jersild, A., Jiang, F., Jin, Z., Kato, E., Keeling, R. F., Klein Goldewijk, K., Knauer, J., Korsbakken, J. I., Lan, X., Lauvset, S. K., Lefèvre, N., Liu, Z., Liu, J., Ma, L., Maksyutov, S., Marland, G., Mayot, N., McGuire, P. C., Metzl, N., Monacci, N. M., Morgan, E. J., Nakaoka, S.-I., Neill, C., Niwa, Y., Nützel, T., Olivier, L., Ono, T., Palmer, P. I., Pierrot, D., Qin, Z., Resplandy, L., Roobaert, A., Rosan, T. M., Rödenbeck, C., Schwinger, J., Smallman, T. L., Smith, S. M., Sospedra-Alfonso, R., Steinhoff, T., Sun, Q., Sutton, A. J., Séférian, R., Takao, S., Tatebe, H., Tian, H., Tilbrook, B., Torres, O., Tourigny, E., Tsujino, H., Tubiello, F., van der Werf, G., Wanninkhof, R., Wang, X., Yang, D., Yang, X., Yu, Z., Yuan, W., Yue, X., Zaehle, S., Zeng, N., and Zeng, J.: Global Carbon Budget 2024, Earth Syst. Sci. Data, 17, 965–1039, https://doi.org/10.5194/essd-17-965-2025, 2025.

Fueglistaler, S. and Haynes, P. H.: Control of interannual and longer-term variability of stratospheric water vapor, J. Geophys. Res., 110, D24108, https://doi.org/10.1029/2005JD006019, 2005.

Gettelman, A., Christensen, M. A., Diamond, M. S., Gryspeerdt, E., Manshausen, P., Sieir, P., Watson-Parris, D., Yang, M., Yoshioka, M., and Yuan, T.: Has Reducing Ship Emissions Brought Forward Global Warming?, Geophys. Res. Lett., 2024.

Gillett, N. P., Shiogama, H., Funke, B., Hegerl, G., Knutti, R., Matthes, K., Santer, B. D., Stone, D., and Tebaldi, C.: The Detection and Attribution Model Intercomparison Project (DAMIP v1.0) contribution to CMIP6, Geosci. Model. Dev., 9, 3685–3697, https://doi.org/10.5194/gmd-9-3685-2016, 2016.

Gillett, N.P., Kirchmeier-Young, M., Ribes, A., Shiogama, H., Hegerl, G.C., Knutti, R., Gastineau, G., John, J.G., Li, L., Nazarenko, L., Rosenbloom, N., Seland, Ø., Wu, T., Yukimoto, S., and Ziehn, T.: Constraining human contributions to observed warming since the pre-industrial period, Nat. Clim. Chang., 11, 207–212, https://doi.org/10.1038/s41558-020-00965-9, 2021.

Good, S. A., Martin, M. J., and Rayner, N. A.: EN4: Quality controlled ocean temperature and salinity profiles and monthly objective analyses with uncertainty estimates, THE EN4 DATA SET, J. Geophys. Res.-Oceans, 118, 6704–6716, https://doi.org/10.1002/2013JC009067, 2013.

Grassi, G., Federici, S., Abad-Vinas, R., Korosuo, A., and Rossi, S.: LULUCF data based on National GHG inventories (NGHGI DB), Zenodo [data set], https://doi.org/10.5281/zenodo.7190601, 2022.

Gulev, S. K., P. W. Thorne, J. Ahn, F. J. Dentener, C. M. Domingues, S. Gerland, D. Gong, D. S. Kaufman, H. C. Nnamchi, J. Quaas, J.A. Rivera, S. Sathyendranath, S.L. Smith, B. Trewin, K. von Schuckmann, and R. S. Vose: Changing State of the Climate System. In Climate Change 2021: The Physical Science Basis. Contribution of Working Group I to the Sixth Assessment Report of the Intergovernmental Panel on Climate Change[Masson-Delmotte, V., P. Zhai, A. Pirani, S.L. Connors, C. Péan, S. Berger, N. Caud, Y. Chen, L. Goldfarb, M.I. Gomis, M. Huang, K. Leitzell, E. Lonnoy, J.B.R. Matthews, T.K. Maycock, T. Waterfield, O. Yelekçi, R. Yu, and B. Zhou (eds.)]. Cambridge University Press, Cambridge, United Kingdom and New York, NY, USA, pp. 287–422, https://doi.org/10.1017/9781009157896.004, 2021.

Granier, C., Darras, S., Denier van der Gon, H., Doubalova, J., Elguindi, N., Galle, B., Gauss, M., Guevara, M., Jalkanen, J.-P., Kuenen, J., Liousse, C., Quack, B., Simpson, D., and Sindelarova, K.: The Copernicus Atmosphere Monitoring Service global and regional emissions (April 2019 version), https://doi.org/10.24380/D0BN-KX16, n.d, 2019.

Gütschow, J., and Busch, D., and Pflüger, M.: The PRIMAP-hist national historical emissions time series v2.6.1 (1750-2023) (2.6.1), Zenodo [data set] https://doi.org/10.5281/zenodo.15016289, 2025.

Jalkanen, J.-P., Johansson, L., Kukkonen, J., Brink, A., Kalli, J., and Stipa, T.: Extension of an assessment model of ship traffic exhaust emissions for particulate matter and carbon monoxide, Atmospheric Chemistry and Physics, 12, 2641–2659, https://doi.org/10.5194/acp-12-2641-2012, 2012.

Jalkanen, J.-P., Johansson, L., and Kukkonen, J.: A comprehensive inventory of ship traffic exhaust emissions in the European sea areas in 2011, Atmos. Chem. Phys., 16, 71–84, https://doi.org/10.5194/acp-16-71-2016, 2016.

Johansson, L., Jalkanen, J.-P., and Kukkonen, J.: Global assessment of shipping emissions in 2015 on a high spatial and temporal resolution, Atmospheric Environment, 167, 403–415, https://doi.org/10.1016/j.atmosenv.2017.08.042, 2017.

Haustein, K., Allen, M. R., Forster, P. M., Otto, F. E. L., Mitchell, D. M., Matthews, H. D., and Frame, D. J.: A real-time Global Warming Index, Sci Rep, 7, 15417, https://doi.org/10.1038/s41598-017-14828-5, 2017.

Hersbach H., Bell, B., Berrisford, P. et al.: The ERA5 global reanalysis, Quat. Jour. R. Met. Soc., 146:1999–2049, https://doi.org/10.1002/qj.3803, 2020.

Hodnebrog, Ø., Myhre, G., Kramer, R. J., Shine, K. P., Andrews, T., Faluvegi, G., Kasoar, M., Kirkevåg, A., Lamarque, J.-F., Mülmenstädt, J., Olivié, D., Samset, B. H., Shindell, D., Smith, C. J., Takemura, T., and Voulgarakis, A.: The effect of rapid adjustments to halocarbons and N2O on radiative forcing, npj Clim. Atmos. Sci., 3, 43, https://doi.org/10.1038/s41612-020-00150-x, 2020a.

Hodnebrog, Ø., Aamaas, B., Fuglestvedt, J. S., Marston, G., Myhre, G., Nielsen, C. J., et al.: Updated global warming potentials and radiative efficiencies of halocarbons and other weak atmospheric absorbers, Rev. Geophys., 58, e2019RG000691, https://doi.org/10.1029/2019RG000691, 2020b.

Hurst, D. F., Oltmans, S. J., Vömel, H., Rosenlof, K. H., Davis, S. M., Ray, E. A., Hall, E. G., and Jordan, A. F.: Stratospheric water vapor trends over Boulder, Colorado: Analysis of the 30 year Boulder record, J. Geophys. Res.-Atmos., 116, https://doi.org/10.1029/2010JD015065, 2011.

Huang, B., Yin, X., Menne, M., Vose, R., and Zhang, H.M.: Improvements to the land surface air temperature reconstruction in NOAA GlobalTemp: An artificial neural network approach, Artificial Intelligence for the Earth Systems, 1, 3, https://journals.ametsoc.org/view/journals/aies/1/4/AIES-D-22-0032.1.xml, 2020.

IATA: Global Outlook for Air Transport: Times of Turbulence, IATA, http://www.iata.org/en/iata-repository/publications/economic-reports/global-outlook-for-air-transport-december-2024/, 2024.

IEA: World oil statistics (Edition 2024), IEA Oil Information Statistics (database), https://doi.org/10.1787/558987b9-en, 2024 (accessed on 24 April 2024).

Ishii, M., Fukuda, Y., Hirahara, S., Yasui, S., Suzuki, T., and Sato, K.: Accuracy of Global Upper Ocean Heat Content Estimation Expected from Present Observational Data Sets, SOLA, 13, 163–167, https://doi.org/10.2151/sola.2017-030, 2017.

Jenkins, S., Smith, C., Allen, M., and Grainger, R.: Tonga eruption increases chance of temporary surface temperature anomaly above 1.5 °C, Nature Clim. Chang., 13, 127–129, https://doi.org/10.1038/s41558-022-01568-2, 2023.

Joshi, M. M. and Jones, G. S.: The climatic effects of the direct injection of water vapour into the stratosphere by large volcanic eruptions, Atmos. Chem. Phys., 9, 6109–6118, https://doi.org/10.5194/acp-9-6109-2009, 2009.

Jungclaus, J. H., Bard, E., Baroni, M., Braconnot, P., Cao, J., Chini, L. P., Egorova, T., Evans, M., González-Rouco, J. F., Goosse, H., Hurtt, G. C., Joos, F., Kaplan, J. O., Khodri, M., Klein Goldewijk, K., Krivova, N., LeGrande, A. N., Lorenz, S. J., Luterbacher, J., Man, W., Maycock, A. C., Meinshausen, M., Moberg, A., Muscheler, R., Nehrbass-Ahles, C., Otto-Bliesner, B. I., Phipps, S. J., Pongratz, J., Rozanov, E., Schmidt, G. A., Schmidt, H., Schmutz, W., Schurer, A., Shapiro, A. I., Sigl, M., Smerdon, J. E., Solanki, S. K., Timmreck, C., Toohey, M., Usoskin, I. G., Wagner, S., Wu, C.-J., Yeo, K. L., Zanchettin, D., Zhang, Q., and Zorita, E.: The PMIP4 contribution to CMIP6 – Part 3: The last millennium, scientific objective, and experimental design for the PMIP4 past1000 simulations, Geosci. Model Dev., 10, 4005–4033, https://doi.org/10.5194/gmd-10-4005-2017, 2017.

Kadow, C., Hall, D. M., and Ulbrich, U.: Artificial intelligence reconstructs missing climate information, Nat. Geosci., 13, 408–413, https://doi.org/10.1038/s41561-020-0582-5, 2020.

Keeble, J., Hassler, B., Banerjee, A., Checa-Garcia, R., Chiodo, G., Davis, S., Eyring, V., Griffiths, P. T., Morgenstern, O., Nowack, P., Zeng, G., Zhang, J., Bodeker, G., Burrows, S., Cameron-Smith, P., Cugnet, D., Danek, C., Deushi, M., Horowitz, L. W., Kubin, A., Li, L., Lohmann, G., Michou, M., Mills, M. J., Nabat, P., Olivié, D., Park, S., Seland, Ø., Stoll, J., Wieners, K.-H., and Wu, T.: Evaluating stratospheric ozone and water vapour changes in CMIP6 models from 1850 to 2100, Atmos. Chem. Phys., 21, 5015–5061, https://doi.org/10.5194/acp-21-5015-2021, 2021.

Kovilakam, M., Thomason, L. W., Ernest, N., Rieger, L., Bourassa, A., and Millán, L.: The Global Space-based Stratospheric Aerosol Climatology (version 2.0): 1979–2018, Earth Syst. Sci. Data, 12, 2607–2634, https://doi.org/10.5194/essd-12-2607-2020, 2020.

Lan, X., Tans, P. and Thoning, K.W.: Trends in globally-averaged CO_2 determined from NOAA Global Monitoring Laboratory measurements, Version Monday, 14-Apr-2025 09:08:57 MDT https://doi.org/10.15138/9N0H-ZH07, 2025.

Leach, N. J., Jenkins, S., Nicholls, Z., Smith, C. J., Lynch, J., Cain, M., Walsh, T., Wu, B., Tsutsui, J., and Allen, M. R.: FaIRv2.0.0: a generalized impulse response model for climate uncertainty and future scenario exploration, Geosci. Model Dev., 14, 3007–3036, https://doi.org/10.5194/gmd-14-3007-2021, 2021.

Lee, D. S., Fahey, D. W., Skowron, A., Allen, M. R., Burkhardt, U., Chen, Q., Doherty, S. J., Freeman, S., Forster, P. M., Fuglestvedt, J., Gettelman, A., León, R. R. D., Lim, L. L., Lund, M. T., Millar, R. J., Owen, B., Penner, J. E., Pitari, G., Prather, M. J., Sausen, R., and Wilcox, L. J.: The contribution of global aviation to anthropogenic climate forcing for 2000 to 2018, Atmos. Environ., 244, 117834, https://doi.org/10.1016/j.atmosenv.2020.117834, 2021.

Lee, J.-Y., J. Marotzke, G. Bala, L. Cao, S. Corti, J.P. Dunne, F. Engelbrecht, E. Fischer, J.C. Fyfe, C. Jones, A. Maycock, J. Mutemi, O. Ndiaye, S. Panickal, and T. Zhou: Future Global Climate: Scenario-Based Projections and Near-Term Information. In Climate Change 2021: The Physical Science Basis. Contribution of Working Group I to the Sixth Assessment Report of the Intergovernmental Panel on Climate Change[Masson-Delmotte, V., P. Zhai, A. Pirani, S.L. Connors, C. Péan, S. Berger, N. Caud, Y. Chen, L. Goldfarb, M.I. Gomis, M. Huang, K. Leitzell, E. Lonnoy, J.B.R. Matthews, T.K. Maycock, T. Waterfield, O. Yelekçi, R. Yu, and B. Zhou (eds.)]. Cambridge University Press, Cambridge, United Kingdom and New York, NY, USA, pp. 553–672,https://doi.org/10.1017/9781009157896.006, 2021.

Lee, H., K. Calvin, D. Dasgupta, G. Krinner, A. Mukherji, P. Thorne, C. Trisos, J. Romero, P. Aldunce, K. Barrett, G. Blanco, W.W.L. Cheung, S.L. Connors, F. Denton, A. Diongue-Niang, D. Dodman, M. Garschagen, O. Geden, B. Hayward, C. Jones, F. Jotzo, T. Krug, R. Lasco, J.-Y. Lee, V. Masson-Delmotte, M. Meinshausen, K. Mintenbeck, A. Mokssit, F.E.L. Otto, M. Pathak, A. Pirani, E. Poloczanska, H.-O. Pörtner, A. Revi, D.C. Roberts, J. Roy, A.C. Ruane, J. Skea, P.R. Shukla, R. Slade, A. Slangen, Y. Sokona, A.A. Sörensson, M. Tignor, D. van Vuuren, Y.-M. Wei, H. Winkler, P. Zhai, and Z. Zommers: Synthesis Report of the IPCC Sixth Assessment Report (AR6): Summary for Policymakers. Intergovernmental Panel on Climate Change [accepted], available at https://www.ipcc.ch/report/ar6/syr/, 2023.

Lenssen, N. J. L., Schmidt, G. A., Hansen, J. E., Menne, M. J., Persin, A., Ruedy, R., and Zyss, D.: Improvements in the GISTEMP Uncertainty Model, J. Geophys. Res.-Atmos., 124, 6307–6326, https://doi.org/10.1029/2018JD029522, 2019.

Levitus, S., Antonov, J. I., Boyer, T. P., Baranova, O. K., Garcia, H. E., Locarnini, R. A., Mishonov, A. V., Reagan, J. R., Seidov, D., Yarosh, E. S., and Zweng, M. M.: World ocean heat content and thermosteric sea level change (0–2000 m), 1955–2010, Geophys. Res. Lett., 39, https://doi.org/10.1029/2012GL051106, 2012.

Matthes, K., Funke, B., Andersson, M. E., Barnard, L., Beer, J., Charbonneau, P., Clilverd, M. A., Dudok de Wit, T., Haberreiter, M., Hendry, A., Jackman, C. H., Kretzschmar, M., Kruschke, T., Kunze, M., Langematz, U., Marsh, D. R., Maycock, A. C., Misios, S., Rodger, C. J., Scaife, A. A., Seppälä, A., Shangguan, M., Sinnhuber, M., Tourpali, K., Usoskin, I., van de Kamp, M., Verronen, P. T., and Versick, S.: Solar forcing for CMIP6 (v3.2), Geosci. Model Dev., 10, 2247–2302, https://doi.org/10.5194/gmd-10-2247-2017, 2017.

Meinshausen, M., Nicholls, Z. R. J., Lewis, J., Gidden, M. J., Vogel, E., Freund, M., Beyerle, U., Gessner, C., Nauels, A., Bauer, N., Canadell, J. G., Daniel, J. S., John, A., Krummel, P. B., Luderer, G., Meinshausen, N., Montzka, S. A., Rayner, P. J., Reimann, S., Smith, S. J., van den Berg, M., Velders, G. J. M., Vollmer, M. K., and Wang, R. H. J.: The shared socio-economic pathway (SSP) greenhouse gas concentrations and their extensions to 2500, Geosci. Model Dev., 13, 3571–3605, https://doi.org/10.5194/gmd-13-3571-2020, 2020.

Millán, L., Santee, M. L., Lambert, A., Livesey, N. J., Werner, F., Schwartz, M. J., Pumphrey, H. C., Manney, G. L., Wang, Y., Su, H., Wu, L., Read, W. G., and Froidevaux, L.: The Hunga Tonga-Hunga Ha'apai Hydration of the Stratosphere, Geophys. Res. Lett., 49, e2022GL099381, https://doi.org/10.1029/2022GL099381, 2022.

Millar, R. J., Nicholls, Z. R., Friedlingstein, P., and Allen, M. R.: A modified impulse-response representation of the global near-surface air temperature and atmospheric concentration response to carbon dioxide emissions, Atmos. Chem. Phys., 17, 7213–7228, https://doi.org/10.5194/acp-17-7213-2017, 2017.

Minx, J. C., Lamb, W. F., Andrew, R. M., Canadell, J. G., Crippa, M., Döbbeling, N., Forster, P. M., Guizzardi, D., Olivier, J., Peters, G. P., Pongratz, J., Reisinger, A., Rigby, M., Saunois, M., Smith, S. J., Solazzo, E., and Tian, H.: A comprehensive and synthetic dataset for global, regional, and national greenhouse gas emissions by sector 1970–2018 with an extension to 2019, Earth Syst. Sci. Data, 13, 5213–5252, https://doi.org/10.5194/essd-13-5213-2021, 2021.

Morice, C. P., Kennedy, J. J., Rayner, N. A., Winn, J. P., Hogan, E., Killick, R. E., Dunn, R. J. H., Osborn, T. J., Jones, P. D., and Simpson, I. R.: An Updated Assessment of Near-Surface Temperature Change From 1850: The HadCRUT5 Data Set, J. Geophys. Res.-Atmos., 126, e2019JD032361, https://doi.org/10.1029/2019JD032361, 2021.

Myhre, G., Samset, B. H., Schulz, M., Balkanski, Y., Bauer, S., Berntsen, T. K., Bian, H., Bellouin, N., Chin, M., Diehl, T., Easter, R. C., Feichter, J., Ghan, S. J., Hauglustaine, D., Iversen, T., Kinne, S., Kirkevåg, A., Lamarque, J.-F., Lin, G., Liu, X., Lund, M. T., Luo, G., Ma, X., van Noije, T., Penner, J. E., Rasch, P. J., Ruiz, A., Seland, Ø., Skeie, R. B., Stier, P., Takemura, T., Tsigaridis, K., Wang, P., Wang, Z., Xu, L., Yu, H., Yu, F., Yoon, J.-H., Zhang, K., Zhang, H., and Zhou, C.: Radiative forcing of the direct aerosol effect from AeroCom Phase II simulations, Atmos. Chem. Phys., 13, 1853–1877, https://doi.org/10.5194/acp-13-1853-2013, 2013a.

Myhre, G., D. Shindell, F.-M. Bréon, W. Collins, J. Fuglestvedt, J. Huang, D. Koch, J.-F. Lamarque, D. Lee, B. Mendoza, T. Nakajima, A. Robock, G. Stephens, T. Takemura and H. Zhang: Anthropogenic and Natural Radiative Forcing. In: Climate Change 2013: The Physical Science Basis. Contribution of Working Group I to the Fifth Assessment Report of the Intergovernmental Panel on Climate Change, edited by Stocker, T.F., D. Qin, G.-K. Plattner, M. Tignor, S.K. Allen, J. Boschung, A. Nauels, Y. Xia, V. Bex and P.M. Midgley (eds.)]. Cambridge University Press, Cambridge, United Kingdom and New York, NY, USA, https://doi.org/10.1017/CBO9781107415324.018, 2013b.

Nicholls Z., Lewis J., Makin M., et al. Regionally aggregated, stitched and de-drifted CMIP-climate data, processed with netCDF-SCM v2.0.0. Geosci Data J., 8, 154–198, https://doi.org/10.1002/gdj3.113, 2021.

Nitzbon, J., Krinner, G., Langer, M.: GCOS EHI 1960-2020 Permafrost Heat Content, World Data Center for Climate (WDCC) at DKRZ, https://doi.org/10.26050/WDCC/GCOS_EHI_1960-2020_PHC, 2022b.

Otto, F. E. L., Frame, D. J., Otto, A., and Allen, M. R.: Embracing uncertainty in climate change policy, Nature Clim. Chang., 5, 917–920, https://doi.org/10.1038/nclimate2716, 2015.

Palmer, M. D., Domingues, C. M., Slangen, A. B. A., and Dias, F. B.: An ensemble approach to quantify global mean sea-level rise over the 20th century from tide gauge reconstructions, Environ. Res. Lett., 16, 044043, https://doi.org/10.1088/1748-9326/abdaec, 2021.

Purkey, S.G. and Johnson, G.C., Warming of Global Abyssal and Deep Southern Ocean Waters between the 1990s and 2000s: Contributions to Global Heat and Sea Level Rise Budgets, J. Climate, 23, 6336–6351, https://doi.org/10.1175/2010JCLI3682.1, 2010.

Prinn, R. G., Weiss, R. F., Arduini, J., Arnold, T., DeWitt, H. L., Fraser, P. J., Ganesan, A. L., Gasore, J., Harth, C. M., Hermansen, O., Kim, J., Krummel, P. B., Li, S., Loh, Z. M., Lunder, C. R., Maione, M., Manning, A. J., Miller, B. R., Mitrevski, B., Mühle, J., O'Doherty, S., Park, S., Reimann, S., Rigby, M., Saito, T., Salameh, P. K., Schmidt, R., Simmonds, P. G., Steele, L. P., Vollmer, M. K., Wang, R. H., Yao, B., Yokouchi, Y., Young, D., and Zhou, L.: History of chemically and radiatively important atmospheric gases from the Advanced Global Atmospheric Gases Experiment (AGAGE), Earth Syst. Sci. Data, 10, 985–1018, https://doi.org/10.5194/essd-10-985-2018, 2018.

Qasmi, S. and Ribes, A.: Reducing uncertainty in local temperature projections, Sci. Adv., 8, eabo6872, https://doi.org/10.1126/sciadv.abo6872, 2022.

Riahi, K., Schaeffer, J. Arango, K. Calvin, C. Guivarch, T. Hasegawa, K. Jiang, E. Kriegler, R. Matthews, G.P. Peters, A. Rao, S. Robertson, A.M. Sebbit, J. Steinberger, M. Tavoni, D.P. van Vuuren, 2022: Mitigation pathways compatible with long-term goals. In IPCC, 2022: Climate Change 2022: Mitigation of Climate Change. Contribution of Working Group III to the Sixth Assessment Report of the Intergovernmental Panel on Climate Change [P.R. Shukla, J. Skea, R. Slade, A. Al Khourdajie, R. van Diemen, D. McCollum, M. Pathak, S. Some, P. Vyas, R. Fradera, M. Belkacemi, A. Hasija, G. Lisboa, S. Luz, J. Malley, (eds.)]. Cambridge University Press, Cambridge, UK and New York, NY, USA, https://doi.org/10.1017/9781009157926.005, 2022.

Ribes, A., Planton, S., and Terray, L.: Application of regularised optimal fingerprinting to attribution. Part I: method, properties and idealised analysis, Clim. Dyn., 41, 2817–2836, https://doi.org/10.1007/s00382-013-1735-7, 2013.

Ribes, A., Qasmi, S., and Gillett, N. P.: Making climate projections conditional on historical observations, Sci. Adv., 7, eabc0671, https://doi.org/10.1126/sciadv.abc0671, 2021.

Richardson, M., Cowtan, K., and Millar, R. J.: Global temperature definition affects achievement of long-term climate goals, Environ. Res. Lett., 13, 054004, https://doi.org/10.1088/1748-9326/aab305, 2018.

Rogelj, J., Schaeffer, M., Meinshausen, M., Shindell, D. T., Hare, W., Klimont, Z., Velders, G. J., Amann, M., and Schellnhuber, H. J.: Disentangling the effects of CO2 and short-lived climate forcer mitigation, Proc. Natl. Acad. Sci. USA, 111 (46), 16325–16330, https://doi.org/10.1073/pnas.1415631111, 2014a.

Rogelj, J., D. Shindell, K. Jiang, S. Fifita, P. Forster, V. Ginzburg, C. Handa, H. Kheshgi, S. Kobayashi, E. Kriegler, L. Mundaca, R. Séférian, and M. V. Vilariño: Mitigation Pathways Compatible with 1.5°C in the Context of Sustainable Development. In: Global Warming of 1.5°C. An IPCC Special Report on the impacts of global warming of 1.5°C above pre-industrial levels and related global greenhouse gas emission pathways, in the context of strengthening the global response to the threat of climate change, sustainable development, and efforts to eradicate poverty [Masson-Delmotte, V., P. Zhai, H.-O. Pörtner, D. Roberts, J. Skea, P.R. Shukla, A. Pirani, W. Moufouma-Okia, C. Péan, R. Pidcock, S. Connors, J. B. R. Matthews, Y. Chen, X. Zhou, M. I. Gomis, E. Lonnoy, T. Maycock, M. Tignor, and T. Waterfield (eds.)]. Cambridge University Press, Cambridge, UK and New York, NY, USA, pp. 93-174, https://doi.org/10.1017/9781009157940.004, 2018.

Rogelj, J., Rao, S., McCollum, D. L., Pachauri, S., Klimont, Z., Krey, V., and Riahi, K: Air-pollution emission ranges consistent with the representative concentration pathways, Nature Clim. Chang., 4 (6), 446–450, https://doi.org/10.1038/nclimate2178, 2014b.

Rogelj, J., Lamboll, R.D.: Substantial reductions in non-CO2 greenhouse gas emissions reductions implied by IPCC estimates of the remaining carbon budget. Communications Earth Environ 5, 35. https://doi.org/10.1038/s43247-023-01168-8, 2024.

Rohde, R., Muller, R., Jacobsen, R., Perlmutter, S., Rosenfeld, A., Wurtele, J., Curry, J., Wickham, C., and Mosher, S.: Berkeley Earth temperature averaging process, Geoinfor. Geostat.: An Overview, 1, https://doi.org/10.4172/2327-4581.1000103, 2013.

Rohde, R. A. and Hausfather, Z.: The Berkeley Earth Land/Ocean Temperature Record, Earth Sys. Sci. Data, 12, 3469–3479, https://doi.org/10.5194/essd-12-3469-2020, 2020.

Sellitto, P., Podglajen, A., Belhadji, R., Boichu, M., Carboni, E., Cuesta, J., Duchamp, C., Kloss, C., Siddans, R., Bègue, N., Blarel, L., Jegou, F., Khaykin, S., Renard, J.B., Legras, B.: The unexpected radiative impact of the Hunga Tonga eruption of 15th January 2022, Commun. Earth. Environ., 3, 288, https://doi.org/10.1038/s43247-022-00618-z, 2022.

von Schuckmann, K., Cheng, L., Palmer, M. D., Hansen, J., Tassone, C., Aich, V., Adusumilli, S., Beltrami, H., Boyer, T., Cuesta-Valero, F. J., Desbruyères, D., Domingues, C., García-García, A., Gentine, P., Gilson, J., Gorfer, M., Haimberger, L., Ishii, M., Johnson, G. C., Killick, R., King, B. A., Kirchengast, G., Kolodziejczyk, N., Lyman, J., Marzeion, B., Mayer, M., Monier, M., Monselesan, D. P., Purkey, S., Roemmich, D., Schweiger, A., Seneviratne, S. I., Shepherd, A., Slater, D. A., Steiner, A. K., Straneo, F., Timmermans, M.-L., and Wijffels, S. E.: Heat stored in the Earth system: where does the energy go?, Earth Syst. Sci. Data, 12, 2013–2041, https://doi.org/10.5194/essd-12-2013-2020, 2020.

von Schuckmann, K., Minière, A., Gues, F., Cuesta-Valero, F. J., Kirchengast, G., Adusumilli, S., Straneo, F., Ablain, M., Allan, R. P., Barker, P. M., Beltrami, H., Blazquez, A., Boyer, T., Cheng, L., Church, J., Desbruyeres, D., Dolman, H., Domingues, C. M., García-García, A., Giglio, D., Gilson, J. E., Gorfer, M., Haimberger, L., Hakuba, M. Z., Hendricks, S., Hosoda, S., Johnson, G. C., Killick, R., King, B., Kolodziejczyk, N., Korosov, A., Krinner, G., Kuusela, M., Landerer, F. W., Langer, M., Lavergne, T., Lawrence, I., Li, Y., Lyman, J., Marti, F., Marzeion, B., Mayer, M., MacDougall, A. H., McDougall, T., Monselesan, D. P., Nitzbon, J., Otosaka, I., Peng, J., Purkey, S., Roemmich, D., Sato, K., Sato, K., Savita, A., Schweiger, A., Shepherd, A., Seneviratne, S. I., Simons, L., Slater, D. A., Slater, T., Steiner, A. K., Suga, T., Szekely, T., Thiery, W., Timmermans, M.-L., Vanderkelen, I., Wjiffels, S. E., Wu, T., and Zemp, M.: Heat stored in the Earth system 1960–2020: where does the energy go?, Earth System Science Data, 15, 1675–1709, https://doi.org/10.5194/essd-15-1675-2023, 2023.

Sigl, M., Toohey, M., McConnell, J. R., Cole-Dai, J., and Severi, M.: Volcanic stratospheric sulfur injections and aerosol optical depth during the Holocene (past 11\,500 years) from a bipolar ice-core array, Earth Syst. Sci. Data, 14, 3167–3196, https://doi.org/10.5194/essd-14-3167-2022, 2022.

Skeie, R. B., Myhre, G., Hodnebrog, Ø., Cameron-Smith, P. J., Deushi, M., Hegglin, M. I., Horowitz, L. W., Kramer, R. J., Michou, M., Mills, M. J., Olivié, D. J. L., Connor, F. M. O., Paynter, D., Samset, B. H., Sellar, A., Shindell, D., Takemura, T., Tilmes, S., and Wu, T.: Historical total ozone radiative forcing derived from CMIP6 simulations, npj Clim. Atmos. Sci., 3, 32, https://doi.org/10.1038/s41612-020-00131-0, 2020.

Smith, C. J., Kramer, R. J., Myhre, G., Forster, P. M., Soden, B. J., Andrews, T., Boucher, O., Faluvegi, G., Fläschner, D., Hodnebrog, Ø., Kasoar, M., Kharin, V., Kirkevåg, A., Lamarque, J.-F., Mülmenstädt, J., Olivié, D., Richardson, T., Samset, B. H., Shindell, D., Stier, P., Takemura, T., Voulgarakis, A., and Watson-Parris, D.: Understanding Rapid Adjustments to Diverse Forcing Agents, Geophys. Res. Lett., 45, 12,023-12,031, https://doi.org/10.1029/2018GL079826, 2018a.

Smith, C. J., Forster, P. M., Allen, M., Leach, N., Millar, R. J., Passerello, G. A., and Regayre, L. A.: FAIR v1.3: A simple emissions-based impulse response and carbon cycle model, Geoscientific Model Development, 11, 2273–2297, https://doi.org/10.5194/gmd-11-2273-2018, 2018b.

Smith, C. J., Harris, G. R., Palmer, M. D., Bellouin, N., Collins, W., Myhre, G., Schulz, M., Golaz, J.-C., Ringer, M., Storelvmo, T., and Forster, P. M.: Energy Budget Constraints on the Time History of Aerosol Forcing and Climate Sensitivity, Journal of Geophysical Research: Atmospheres, 126, e2020JD033622, https://doi.org/10.1029/2020JD033622, 2021a.

Smith, C., Nicholls, Z. R. J., Armour, K., Collins, W., Forster, P., Meinshausen, M., Palmer, M. D., and Watanabe, M.: The Earth's Energy Budget, Climate Feedbacks, and Climate Sensitivity Supplementary Material, in: Climate Change 2021: The Physical Science Basis. Contribution of Working Group I to the Sixth Assessment Report of the Intergovernmental Panel on Climate Change, edited by: Masson-Delmotte, V., Zhai, P., Pirani, A., Connors, S. L., Péan, C., Berger, S., Caud, N., Chen, Y., Goldfarb, L., Gomis, M. I., Huang, M., Leitzell, K., Lonnoy, E., Matthews, J. B. R., Maycock, T. K., Waterfield, T., Yelekçi, O., Yu, R., and Zhou, B., 2021b.

Smith, C., Cummins, D. P., Fredriksen, H.-B., Nicholls, Z., Meinshausen, M., Allen, M., Jenkins, S., Leach, N., Mathison, C., and Partanen, A.-I.: fair-calibrate v1.4.1: calibration, constraining, and validation of the FaIR simple climate model for reliable future climate projections, Geosci. Model Dev., 17, 8569–8592, https://doi.org/10.5194/gmd-17-8569-2024, 2024.

Stevenson, D. S., Young, P. J., Naik, V., Lamarque, J.-F., Shindell, D. T., Voulgarakis, A., Skeie, R. B., Dalsoren, S. B., Myhre, G., Berntsen, T. K., Folberth, G. A., Rumbold, S. T., Collins, W. J., MacKenzie, I. A., Doherty, R. M., Zeng, G., van Noije, T. P. C., Strunk, A., Bergmann, D., Cameron-Smith, P., Plummer, D. A., Strode, S. A., Horowitz, L., Lee, Y. H., Szopa, S., Sudo, K., Nagashima, T., Josse, B., Cionni, I., Righi, M., Eyring, V., Conley, A., Bowman, K. W., Wild, O., and Archibald, A.: Tropospheric ozone changes, radiative forcing and attribution to emissions in the Atmospheric Chemistry and Climate Model Intercomparison Project (ACCMIP), Atmos. Chem. Phys., 13, 3063–3085, https://doi.org/10.5194/acp-13-3063-2013, 2013.

Steiner, A. K., Ladstädter, F., Randel, W. J., Maycock, A. C., Fu, Q., Claud, C., Gleisner, H., Haimberger, L., Ho, S.-P., Keckhut, P., Leblanc, T., Mears, C., Polvani, L. M., Santer, B. D., Schmidt, T., Sofieva, V., Wing, R., and Zou, C.-Z.: Observed Temperature Changes in the Troposphere and Stratosphere from 1979 to 2018, J. Climate, 33, 8165–8194, https://doi.org/10.1175/JCLI-D-19-0998.1, 2020.

Sun, W., Li, Q., Huang, B., Cheng, J., Song, Z., Li, H., Dong, W., Zhai, P., and Jones, P.: The Assessment of Global Surface Temperature Change from 1850s: The C-LSAT2.0 Ensemble and the CMST-Interim Datasets, Advances in Atmospheric Sciences, 38, 875–888, https://doi.org/10.1007/s00376-021-1012-3, 2021.

Szopa, S., V. Naik, B. Adhikary, P. Artaxo, T. Berntsen, W.D. Collins, S. Fuzzi, L. Gallardo, A. Kiendler-Scharr, Z. Klimont, H. Liao, N. Unger, and P. Zanis: Short-Lived Climate Forcers. In Climate Change 2021: The Physical Science Basis. Contribution of Working Group I to the Sixth Assessment Report of the Intergovernmental Panel on Climate Change [Masson-Delmotte, V., P. Zhai, A. Pirani, S.L. Connors, C. Péan, S. Berger, N. Caud, Y. Chen, L. Goldfarb, M.I. Gomis, M. Huang, K. Leitzell, E. Lonnoy, J.B.R. Matthews, T.K. Maycock, T. Waterfield, O. Yelekçi, R. Yu, and B. Zhou (eds.)]. Cambridge University Press, Cambridge, United Kingdom and New York, NY, USA, pp. 817–922, https://doi:10.1017/9781009157896.008, 2021.

Taha, G., Loughman, R., Zhu, T., Thomason, L., Kar, J., Rieger, L., and Bourassa, A.: OMPS LP Version 2.0 multi-wavelength aerosol extinction coefficient retrieval algorithm, Atmos. Meas. Tech., 14, 1015–1036, https://doi.org/10.5194/amt-14-1015-2021, 2021.

Taylor, K. E., Crucifix, M., Braconnot, P., Hewitt, C. D., Doutriaux, C., Broccoli, A. J., Mitchell, J. F. B., and Webb, M. J.: Estimating Shortwave Radiative Forcing and Response in Climate Models, J. Climate, 20, 2530–2543, https://doi.org/10.1175/JCLI4143.1, 2007.

Thomason, L. W., Ernest, N., Millán, L., Rieger, L., Bourassa, A., Vernier, J.-P., Manney, G., Luo, B., Arfeuille, F., and Peter, T.: A global space-based stratospheric aerosol climatology: 1979–2016, Earth Syst. Sci. Dat., 10, 469–492, https://doi.org/10.5194/essd-10-469-2018, 2018.

Thornhill, G. D., Collins, W. J., Kramer, R. J., Olivié, D., Skeie, R. B., O'Connor, F. M., Abraham, N. L., Checa-Garcia, R., Bauer, S. E., Deushi, M., Emmons, L. K., Forster, P. M., Horowitz, L. W., Johnson, B., Keeble, J., Lamarque, J.-F., Michou, M., Mills, M. J., Mulcahy, J. P., Myhre, G., Nabat, P., Naik, V., Oshima, N., Schulz, M., Smith, C. J., Takemura, T., Tilmes, S., Wu, T., Zeng, G., and Zhang, J.: Effective radiative forcing from emissions of reactive gases and aerosols – a multi-model comparison, Atmos. Chem. Phys., 21, 853–874, https://doi.org/10.5194/acp-21-853-2021, 2021a.

Thornhill, G., Collins, W., Olivié, D., Skeie, R. B., Archibald, A., Bauer, S., Checa-Garcia, R., Fiedler, S., Folberth, G., Gjermundsen, A., Horowitz, L., Lamarque, J.-F., Michou, M., Mulcahy, J., Nabat, P., Naik, V., O'Connor, F. M., Paulot, F., Schulz, M., Scott, C. E., Séférian, R., Smith, C., Takemura, T., Tilmes, S., Tsigaridis, K., and Weber, J.: Climate-driven chemistry and aerosol feedbacks in CMIP6 Earth system models, Atmos. Chem. Phys., 21, 1105–1126, https://doi.org/10.5194/acp-21-1105-2021, 2021b.

Toohey, M. and Sigl, M.: Volcanic stratospheric sulfur injections and aerosol optical depth from 500\,BCE to 1900\,CE, Earth Syst. Sci. Data, 9, 809–831, https://doi.org/10.5194/essd-9-809-2017, 2017.

Trewin, B., Cazenave, A., Howell, S., Huss, M., Isensee, K., Palmer, M. D., Tarasova, O., and Vermeulen, A.: Headline Indicators for Global Climate Monitoring, Bulletin of the American Meteorological Society, 102, E20–E37, https://doi.org/10.1175/BAMS-D-19-0196.1, 2021.

Vanderkelen, I., van Lipzig, N. P. M., Lawrence, D. M., Droppers, B., Golub, M., Gosling, S. N., Janssen, A. B. G., Marcé, R., Schmied, H. M., Perroud, M., Pierson, D., Pokhrel, Y., Satoh, Y., Schewe, J., Seneviratne, S. I., Stepanenko, V. M., Tan, Z., Woolway, R. I., and Thiery, W.: Global Heat Uptake by Inland Waters, Geophysical Research Letters, 47, e2020GL087867, https://doi.org/10.1029/2020GL087867, 2020.

Vose, R. S., Huang, B., Yin, X., Arndt, D., Easterling, D. R., Lawrimore, J. H., Menne, M. J., Sanchez-Lugo, A., and Zhang, H. M.: Implementing Full Spatial Coverage in NOAA's Global Temperature Analysis, Geophys. Res. Lett., 48, e2020GL090873, https://doi.org/10.1029/2020GL090873, 2021.

Watson-Parris, D., Christensen, M. W., Laurenson, A., Clewley, D., Gryspeerdt, E., and Stier, P.: Shipping regulations lead to large reduction in cloud perturbations, Proc. Natl. Acad. Sci. U.S.A., 119, e2206885119, https://doi.org/10.1073/pnas.2206885119, 2022.

van der Werf, G. R., Randerson, J. T., Giglio, L., van Leeuwen, T. T., Chen, Y., Rogers, B. M., Mu, M., van Marle, M. J. E., Morton, D. C., Collatz, G. J., Yokelson, R. J., and Kasibhatla, P. S.: Global fire emissions estimates during 1997–2016, Earth System Science Data, 9, 697–720, https://doi.org/10.5194/essd-9-697-2017, 2017.

World Meteorological Organization (WMO), 2025. State of the Global Climate 2024. WMO-No. 1368. World Meteorological Organization, https://library.wmo.int/idurl/4/69455, accessed 27 April 2025, 2025.

Yuan, T., Song, H., Wood, R., Wang, C., Oreopoulos, L., Platnick, S. E., Von Hippel, S., Meyer, K., Light, S., and Wilcox, E.: Global reduction in ship-tracks from sulfur regulations for shipping fuel, Sci. Adv., 8, eabn7988, https://doi.org/10.1126/sciadv.abn7988, 2022.

Zelinka, M. D., Andrews, T., Forster, P. M., and Taylor, K. E.: Quantifying components of aerosol-cloud-radiation interactions in climate models, J. Geophys. Res.-Atmos., 119, 7599–7615, https://doi.org/10.1002/2014JD021710, 2014.

Zelinka, M. D., Smith, C. J., Qin, Y., and Taylor, K. E.: Aerosol Effective Radiative Forcings in CMIP Models, EGUsphere, https://acp.copernicus.org/articles/23/8879/2023, 2023.